

Generative Modeling of Full-Atom Protein Conformations using Latent Diffusion on Graph Embeddings

Aditya Sengar^{*†‡}
aditya.sengar@epfl.ch

Ali Hariri^{*}
ali.hariri@epfl.ch

Daniel Probst[§]
daniel.probst@wur.nl

Patrick Barth[¶]
patrick.barth@epfl.ch

Pierre Vandergheynst^{*}
pierre.vandergheynst@epfl.ch

Abstract

Generating diverse, all-atom conformational ensembles of dynamic proteins such as G-protein-coupled receptors (GPCRs) is critical for understanding their function, yet most generative models simplify atomic detail or ignore conformational diversity altogether. We present latent diffusion for full protein generation (LD-FPG), a framework that constructs complete all-atom protein structures, including every side-chain heavy atom, directly from molecular dynamics (MD) trajectories. LD-FPG employs a Chebyshev graph neural network (ChebNet) to obtain low-dimensional latent embeddings of protein conformations, which are processed using three pooling strategies: blind, sequential and residue-based. A diffusion model trained on these latent representations generates new samples that a decoder, optionally regularized by dihedral-angle losses, maps back to Cartesian coordinates. Using D2R-MD, a 2 μ s MD trajectory (12 000 frames) of the human dopamine D2 receptor in a membrane environment, the sequential and residue-based pooling strategy reproduces the reference ensemble with high structural fidelity (all-atom IDDT ~ 0.7 ; $C\alpha$ -IDDT ~ 0.8) and recovers backbone and side-chain dihedral-angle distributions with a Jensen–Shannon divergence < 0.03 compared to the MD data. LD-FPG thereby offers a practical route to system-specific, all-atom ensemble generation for large proteins, providing a promising tool for structure-based therapeutic design on complex, dynamic targets. The D2R-MD dataset and our implementation are freely available to facilitate further research.

1 Introduction

Proteins function as dynamic molecular machines whose biological activities critically depend on transitioning between distinct conformational states [1, 2]. Landmark artificial intelligence methods like AlphaFold2 [3] and others [4–7] have advanced structure prediction but predominantly predict single static conformations, limiting their utility for systems with conformational heterogeneity. Accurate modeling of an ensemble of accessible conformations is essential to elucidate protein function and guide therapeutic design [8–11]. Crucially, these ensembles must explicitly represent all

^{*}Signal Processing Laboratory (LTS2), EPFL, Lausanne, Switzerland

[†]Institute of Bioengineering, EPFL, Lausanne, Switzerland

[‡]Corresponding author

[§]Bioinformatics Group, University & Research Wageningen, The Netherlands

[¶]Ludwig Institute for Cancer Research, Lausanne, Switzerland

atomic details, particularly side chains, whose subtle conformational rearrangements often govern molecular recognition and catalytic mechanisms [12].

Despite rapid advancements, existing generative models frequently fall short in capturing the detailed dynamics of side-chain movements specific to particular proteins [13]. Many powerful methodologies have focused either on *de novo* backbone designs [14–16] or on generating static all-atom structures [17, 18], but neither produce comprehensive conformational ensembles. Ensemble-generating approaches—via perturbations of static predictors [19, 20], flow-matched variants [21], or general MD-trained generators [22, 23]—typically operate at the backbone or coarse-grained level. Consequently, they fail to capture the intricate all-atom rearrangements, particularly involving side chains, that are critical for function. Although promising latent space [24–26] and physics-informed models [27, 28] have emerged, their capability to generate high-resolution all-atom ensembles from MD data reflecting functional transitions remains unproven, highlighting a significant unmet need for specialized generative frameworks.

G protein-coupled receptors (GPCRs) provide a compelling example of dynamic systems wherein precise all-atom modeling is indispensable [29]. This large family of transmembrane receptors, comprising over 800 human members, is responsible for mediating most known transmembrane signal transduction [30, 31] and is targeted by approximately 50% of all marketed drugs [32, 33]. GPCR signaling involves conformational transitions among multiple states, frequently induced by ligand binding [34], and occurs through intricate allosteric mechanisms where specific side-chain interactions are crucial [35, 36]. Capturing such dynamic, atomically detailed landscapes is vital to understanding receptor signaling specificity [37], biased agonism [38], and the design of drugs targeting unique allosteric sites [39–41], yet studying these events computationally remains formidable [42–44]. Current predictive methods for GPCR dynamics [45] do not generate the comprehensive all-atom conformational landscapes essential for mechanistic understanding.

To address this critical requirement, we introduce *Latent Diffusion for Full Protein Generation (LD-FPG)*, a generative framework designed to **learn and generate diverse, all-atom conformational ensembles from existing MD simulation data of a target protein**, explicitly including side-chain details. Rather than simulating new trajectories, LD-FPG leverages extensive MD datasets. Our approach employs a Chebyshev Spectral Graph Convolutional Network (ChebNet) [46] to encode all-atom MD snapshots into a compact latent representation. A Denoising Diffusion Probabilistic Model (DDPM) [47] is then trained to explore this learned latent manifold, and latent representations are decoded back into full all-atom Cartesian coordinates. We demonstrate our framework on extensive MD simulations of the human dopamine D2 receptor (D2R), systematically evaluating distinct decoder pooling strategies. Our primary contributions in this paper are:

1. To the best of our knowledge, we present the first latent diffusion modeling framework specifically tailored to generate *complete, all-atom protein conformational ensembles*, capturing both backbone and **side-chain** dynamics directly from MD simulations.
2. We introduce and critically evaluate a novel graph-based autoencoder architecture utilizing ChebNet combined with distinct decoder pooling strategies, offering insights into dynamic protein ensemble generation.
3. Using the D2R system, we demonstrate our method’s ability to generate high-fidelity ensembles, highlight the advantages of residue-based pooling, and assess the impact of auxiliary dihedral loss terms on generative accuracy.

Our approach provides a computationally efficient tool for exploring complex dynamics in switchable proteins, supporting both fundamental mechanistic studies and drug discovery applications. The remainder of this paper is structured as follows: Section 2 reviews related work; Section 3 details our proposed methodology; Section 4 presents the experimental setup and results; and Section 5 summarizes our findings and outlines future directions.

2 Related Work

Generative Models for Protein Design and Static Structure Prediction. Deep generative models have made significant strides in protein science, employing techniques such as diffusion [47], flow-matching [48, 49], and learned latent spaces [24, 50] to tackle complex structural tasks. For *de novo* backbone design, various methods, often inspired by the success of predictors like AlphaFold2

[3] and diffusion-based approaches like RFdiffusion [14] have emerged. Notable examples include FoldingDiff [15], alongside flow-matching models such as FoldFlow2 [49]. Latent space strategies have also been pivotal in this domain; for instance, LatentDiff [24] generates novel protein backbones using an equivariant diffusion model within a condensed latent space, while Ig-VAE [50] utilizes a variational autoencoder for class-specific backbone generation (e.g., for immunoglobulins). While powerful for creating new folds (e.g., Proteina [16]) or specific components, these methods typically target soluble proteins, often generate only backbone coordinates, and are not primarily designed for sampling multiple conformations of a specific, existing protein. The generation of complete static all-atom structures has also seen considerable progress. Models like Protpardelle [17] and Chroma [18] can produce full static structures from sequence information. Diffusion-based generative models such as AlphaFold3 [6] and Boltz-1 [7] also provide detailed single-state predictions of all-atom structures and complexes. Other approaches, like PLAID [25], integrate predictors with diffusion samplers. To complement backbone or static generation, methods including FlowPacker [51] and SidechainDiff [52] focus on side-chain packing or prediction. However, these tools predominantly yield single static structures. Furthermore, decoupling backbone and side-chain generation risks overlooking their critical interplay during the complex dynamic transitions [29] relevant to the conformational landscapes our work aims to capture.

Modeling Protein Conformational Diversity: From General Strategies to MD-Informed Approaches. Beyond single static structures, capturing a protein’s conformational diversity is crucial for understanding its function. Initial strategies to explore this diversity include learning from structural variations in experimental databases (e.g., Str2Str [20]) or perturbing static predictions to sample conformational space, as seen with AF2-RAVE [19] for GPCRs and AlphaFlow/ESMFlow [21] more broadly. While these methods effectively broaden sampling, capturing system-specific, native-like dynamics often benefits from models trained directly on simulation data, which can provide a richer representation of a given protein’s accessible states. Among such simulation-informed approaches, latent space models have shown promise. For example, EnsembleVAE [53], trained on MD snapshots and crystal structures of the soluble protein K-Ras, generates C_α ensembles from sampled latent features with full-atom picture subsequently produced by RoseTTAFold [4]. Similarly, idpSAM [26], trained on extensive simulations of intrinsically disordered regions (IDRs) with an implicit solvent model, produces C_α trace ensembles that can then be converted to all-atom representations. Such approaches demonstrate the power of leveraging simulation data within generative frameworks, though their application has often focused on particular protein classes (e.g., soluble proteins, IDRs) or involved multi-stage processes for generating final all-atom structures. Further advancements in learning ensembles directly from MD simulations encompass a range of techniques. These include methods like ConfDiff [27] (force-guided diffusion), P2DFlow [54] (SE(3) flow matching), and MD-Gen [55] (continuous trajectories). Larger-scale models such as BioEmu [22] and Distributional Graphormer (DiG) [23] aim to learn from vast MD datasets or equilibrium distributions, while experimentally-guided approaches like EGDiff [28] integrate diverse data types. Collectively, these MD-informed methods signify substantial progress in modeling protein dynamics. However, a persistent challenge, particularly when these methods are applied generally or to very large datasets, is the consistent generation of high-resolution, all-atom ensembles that fully capture system-specific details. This is especially true for intricate side-chain rearrangements within native environments, such as lipid membranes for G protein-coupled receptors (GPCRs), which are essential for elucidating their functional transitions [29]. The development of generative models that can directly learn and sample such specific, all-atom conformational landscapes from relevant MD data, particularly for complex targets like GPCRs [44], thus remains an important frontier.

3 Methodology

The LD-FPG framework (Fig. 1) generates diverse, all-atom conformational ensembles of a specific protein by learning to sample deformations relative to a reference structure, X_{ref} . Our approach employs an encoder (Section 3.2) to map protein conformations into atom-wise latent embeddings representing these deformations. These high-dimensional embeddings are then processed by a pooling strategy (detailed in Section 3.3) to create a compact latent representation, \mathbf{h}_0 . A diffusion model (Section 3.4) is trained to sample this lower-dimensional pooled latent space. Finally, a decoder (Section 3.3), conditioned on reference information derived from X_{ref} (see Conditioning Mechanism in Section 3.2), maps these sampled pooled latents back to full all-atom Cartesian coordinates. This strategy simplifies generation by focusing on learning dynamic changes around a known fold.

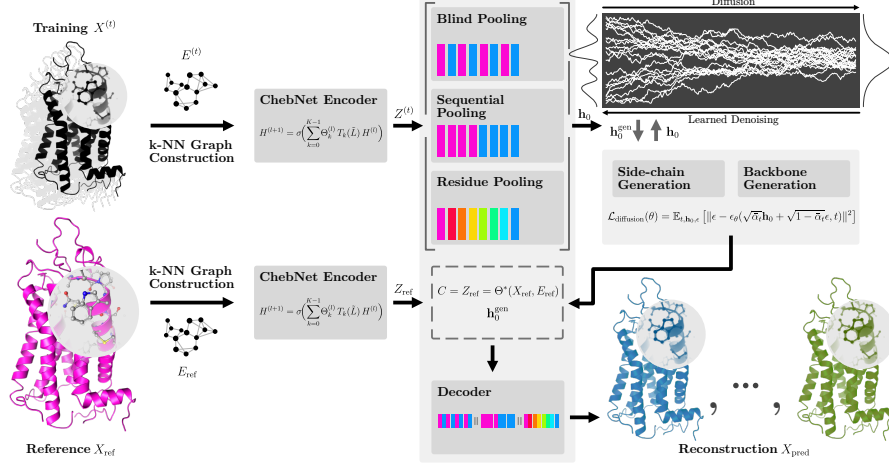


Figure 1: **Schematic of the LD-FPG framework.** The workflow depicts: (1) ChebNet encoding of MD frames to atom-wise latent embeddings ($Z^{(t)}$). (2) Pooling of $Z^{(t)}$ into a compact latent context (h_0). (3) DDPM-based sampling of this pooled latent space to generate h_0^{gen} . (4) Decoding of h_0^{gen} , conditioned on reference latents (Z_{ref}), to all-atom coordinates (X_{pred}). The conceptual details of the framework are described in Section 3.

Appendix A details the overall algorithm and notation used throughout this work. Further methodological details for each component are provided across Appendices B through E, covering aspects from input representation to loss definitions. All specific architectural parameters, model configurations, and hyperparameter optimization scans are consolidated in the Extended Technical Appendix (Appendix I).

3.1 Input Representation and Preprocessing

Each MD snapshot t is represented by a graph $G^{(t)} = (V, E^{(t)})$, where the node set V comprises the N heavy atoms and the node features are their 3D coordinates $X^{(t)} \in \mathbb{R}^{N \times 3}$. For each frame, the edge index $E^{(t)}$ is built on the fly by applying a k -Nearest Neighbors search to the aligned coordinates $X^{(t)}$ with $k = 4$, see Extended Technical Appendix I. The node positions serve both as input features and regression targets. Prior to graph construction, the raw MD coordinates $\tilde{X}^{(t)}$ are rigid-body aligned to the first frame using the Kabsch algorithm [56] to remove global rotation and translation.

3.2 Latent learning of conformations

Multi-hop encoding: For each MD frame t , the encoder Θ maps the Kabsch-aligned heavy-atom coordinates $X^{(t)}$ and their k -NN graph $E^{(t)}$ to latent embeddings $Z^{(t)} \in \mathbb{R}^{N \times d_z}$, one d_z -dimensional vector per heavy atom. We implement Θ as a four-layer ChebNet [46] whose layers perform spectral graph convolutions with Chebyshev polynomials of order $K = 4$:

$$H^{(l+1)} = \sigma \left(\sum_{k=0}^{K-1} \Theta_k^{(l)} T_k(\tilde{L}) H^{(l)} \right), \quad (1)$$

where $H^{(l)} \in \mathbb{R}^{N \times F_l}$ are the node features at layer l ($H^{(0)} = X^{(t)}$), \tilde{L} is the scaled graph Laplacian, $T_k(\cdot)$ is the k^{th} Chebyshev polynomial, $\Theta_k^{(l)} \in \mathbb{R}^{F_l \times F_{l+1}}$ are learnable weights, and σ denotes a Leaky/ReLU non-linearity. Each layer is followed by BatchNorm, and the final output is L_2 -normalised per atom to yield $Z^{(t)}$. The embedding dimension d_z was tuned; the best trade-off was obtained with $d_z=16$ for blind pooling, 8 for sequential pooling, and 4 for residue pooling.

Conditioning Mechanism: Each generated conformation is expressed as a deformation of a *reference* structure: the first Kabsch-aligned MD frame, (X_{ref}, E_{ref}) . Rather than conditioning on raw Cartesian coordinates, we feed the decoder the reference’s latent representation $C = Z_{ref} =$

$\Theta^*(X_{\text{ref}}, E_{\text{ref}})$ where Θ^* denotes the frozen, pre-trained encoder parameters. This embedding compactly summarizes both 3-D geometry and graph topology, and in ablation studies outperformed using X_{ref} directly. At generation time we copy C to every sample in the batch, C_{ex} ; the diffusion model then predicts only the atomic *displacements* from this common reference. This simplifies learning and guarantees that all sampled conformations stay anchored in the same chemical frame.

3.3 Decoder Architectures and Pooling Strategies

The decoder maps atom-wise latent embeddings $Z^{(t)} \in \mathbb{R}^{N \times d_z}$ (representing conformational deformations from X_{ref} , output by the encoder detailed in Section 3.2) and a conditioner $C \in \mathbb{R}^{N \times d_c}$ to all-atom coordinates $X_{\text{pred}} \in \mathbb{R}^{N \times 3}$. While these $Z^{(t)}$ embeddings are information-rich (as demonstrated in Section 4.2), their high dimensionality (e.g., up to $35k$ for D2R with $d_z = 16$) makes them computationally challenging for direct use as input to a diffusion model. Therefore, $Z^{(t)}$ is processed via a pooling strategy to yield a much more compact latent representation, \mathbf{h}_0 (typically $d_p \approx 60 - 100$ for Blind and Sequential strategies), which serves as the substrate for the diffusion model (Section 3.4). This compression is crucial, as preliminary experiments showed that $d_p > 200 - 300$ hampered diffusion training (for blind and sequential), while $d_p < 50$ degraded reconstruction quality. The efficacy of LD-FPG thus relies on the pooling strategy’s ability to generate an informative yet compact \mathbf{h}_0 . We investigate three strategies: Blind pooling, sequential pooling, and residue-based pooling.

Blind pooling: Atom-wise embeddings are globally pooled across all N atoms using 2D adaptive average pooling $\mathcal{P}_{\text{global}}$ (reshaping $Z^{(t)}$ as an image-like tensor of size $N \times d_z$), yielding one context vector $z_{\text{global}} \in \mathbb{R}^{d_p}$ per sample in the batch (where $d_p = H \times W$ from the pooling dimensions). This global vector is tiled for each atom and concatenated with the corresponding broadcast conditioner vector $C^{(i)}$ to form the input $M_{\text{in}}^{(i)}$ for a shared MLP, $\text{MLP}_{\text{blind}}$, which predicts all atom coordinates X_{pred} simultaneously.

Sequential pooling: Decoding is split into two stages. A *BackboneDecoder* first processes $Z^{(t)}$ and C to output backbone coordinates X_{bb} . It typically pools backbone-specific embeddings to form a backbone context. Subsequently, a *SidechainDecoder* predicts side-chain coordinates X_{sc} using $Z^{(t)}$, C , and the predicted X_{bb} . This stage often involves pooling sidechain-specific embeddings and combining this with backbone information and parts of the conditioner to form features for an MLP. The final structure is $X_{\text{pred}} = [X_{\text{bb}} \parallel X_{\text{sc}}]$. Three SidechainDecoder variants (arch-types 0–2) explore different feature constructions for the sidechain prediction MLP.

Residue-based pooling: This strategy models conformational changes as residue-level deformations relative to X_{ref} . For each residue R_j , its constituent atom embeddings $Z_{R_j}^{(t)}$ (a subset of the overall atom-wise deformations $Z^{(t)}$) represent its specific deformation from the reference state implicitly provided by Z_{ref} . These $Z_{R_j}^{(t)}$ are pooled via \mathcal{P}_{res} into a local context vector $z_{\text{res},j} \in \mathbb{R}^{d_p}$, which summarizes residue R_j ’s deformation. Each atom i (in residue $R_{f(i)}$) then receives $z_{\text{res},f(i)}$ concatenated with its reference latent $C^{(i)}$ (from Z_{ref}) as input to MLP_{res} for coordinate prediction. Thus, the decoder reconstructs atom positions from these summaries of residue-specific deformations relative to the reference.

3.4 Latent Diffusion Model for Generation

A Denoising Diffusion Probabilistic Model (DDPM) [47] operates on the pooled latent embeddings \mathbf{h}_0 derived from the chosen decoder pooling strategy. The model is trained to predict the noise ϵ that was added during a forward diffusion process. This training minimizes the standard DDPM loss function, $\mathcal{L}_{\text{diffusion}}$ (Eq. 2). New latent representations, $\mathbf{h}_0^{\text{gen}}$, are then sampled by iteratively applying the learned denoising network in a reverse diffusion process.

$$\mathcal{L}_{\text{diffusion}}(\theta) = \mathbb{E}_{t, \mathbf{h}_0, \epsilon} [\|\epsilon - \epsilon_\theta(\sqrt{\alpha_t} \mathbf{h}_0 + \sqrt{1 - \alpha_t} \epsilon, t)\|^2] \quad (2)$$

3.5 Loss Functions

The LD-FPG framework uses a series of MSE-based losses to train its encoder and decoders. A pre-trained encoder Θ minimizes a coordinate reconstruction MSE (\mathcal{L}_{HNO}), while all decoders focus on coordinate accuracy: Blind pooling begins with $\mathcal{L}_{\text{coord}}$ and, if fine-tuned, applies a weighted composite $\mathcal{L}_{\text{Dec}} = w_{\text{base}}\mathcal{L}_{\text{coord}} + \lambda_{\text{mse}}\mathcal{L}_{\text{mse_dih}} + \lambda_{\text{div}}\mathcal{L}_{\text{div_dih}}$ (the latter two dihedral terms used stochastically only for this strategy), Residue-based Pooling uses $\mathcal{L}_{\text{Dec}} = \mathcal{L}_{\text{coord}}$, and Sequential Pooling optimizes backbone and sidechain predictions in two stages via separate MSE losses \mathcal{L}_{BB} and \mathcal{L}_{SC} .

4 Experimental Setup

4.1 Experimental Setup

D2 Receptor Dynamics dataset: We perform extensive all-atom Molecular Dynamics (MD) simulations of the human Dopamine D2 receptor (D2R) to generate the input dataset. The system, comprising the D2R (2191 heavy atoms) embedded in a POPC membrane with water and ions, was simulated using GROMACS. The final dataset consists of 12,241 frames sampled every 100 ps after discarding initial equilibration. All frames were aligned to the first frame using the Kabsch algorithm. The data was then split into training (90%) and test (10%) sets. Static topology information, including atom indexing and dihedral angle definitions, was pre-processed. Further details on the simulation protocol, system preparation, and data pre-processing are provided in Appendix F.1 and Appendix B.

Evaluation Metrics. Model performance is assessed using metrics evaluating coordinate accuracy (e.g., MSE, IDDT, TM-score), dihedral angle distributional accuracy ($\sum \text{JSD}$), physical plausibility (steric clashes), and conformational landscape sampling (e.g., A100 activation index [57], PCA of latent embeddings). Auxiliary dihedral training losses are also reported where applicable for specific decoder configurations. Detailed definitions and calculation methods for all evaluation metrics are provided in Appendix F.2.

Implementation Details. All models were implemented in PyTorch [58] and trained using the Adam optimizer [59]. The overall three-phase training and generation workflow (encoder pre-training, decoder training, and diffusion model training) is detailed in Appendix A (Algorithm 1).

4.2 Results and Analysis

We evaluated LD-FPG’s ability to generate high-fidelity, all-atom protein conformational ensembles via a multi-stage analysis: (1) assessing ChebNet encoder quality to establish an upper fidelity bound; (2) analyzing decoder reconstruction from ground-truth latents to isolate decoder errors; and (3) evaluating conformational ensembles from the full latent diffusion pipeline. Model IDDT scores (vs. X_{ref}) are interpreted against the “Ground Truth (MD) Ref” IDDT (Tables 1, Appendix G), which reflects the MD ensemble’s average internal diversity relative to X_{ref} . Scores near this MD benchmark suggest a good balance of structural fidelity and diversity; significantly lower scores imply poorer fidelity, while substantially higher scores (approaching 1.0) might indicate insufficient diversity and over-similarity to X_{ref} .

Table 1: Decoder Reconstruction Performance

Decoder Configuration	IDDT _{All} ↑	IDDT _{BB} ↑	TM _{All} ↑	$\sum \text{JSD}_{\text{bb}}$ ↓	$\sum \text{JSD}_{\text{sc}}$ ↓	MSE _{bb} ↓	MSE _{sc} ↓	$\sum \mathcal{L}_{\text{dih}}$ MSE ↓
Blind pooling ($d_z = 16$)	0.714	0.792	0.961	0.0032	0.0290	0.1102	0.3934	0.3802
+ Dih. Fine-tuning	0.698	0.776	0.960	0.0029	0.0279	0.0971	0.3564	0.2849
Seq. pooling ($d_z = 8$)	0.718	0.800	0.961	0.0026	0.0192	0.1291	0.5130	0.5164
Residue pooling ($d_z = 4$)	0.704	0.777	0.962	0.0078	0.0125	0.083	0.2257	0.2163
Ground Truth (MD) Ref	0.698	0.779	0.959	-	-	-	-	-

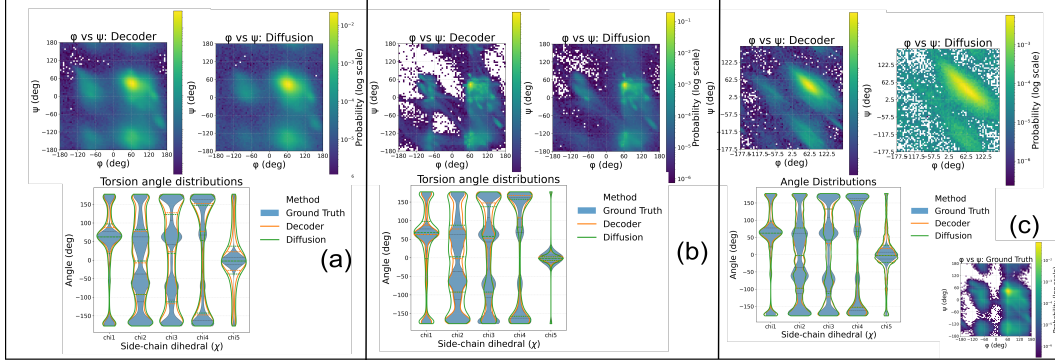


Figure 2: Comparison of dihedral angle distributions for different pooling strategies. (Top row) Ramachandran plots (ϕ vs ψ , log probability) comparing Decoder Reconstruction (left) and Diffusion Generation (right) outputs. (Bottom row) Violin plots comparing 1D sidechain dihedral angle (χ_1 – χ_5) distributions for Ground Truth (MD, blue), Decoder Reconstruction (orange), and Diffusion Generation (green). (a) Blind pooling. (b) Sequential pooling. (c) Residue pooling.

Multi-hop encoding fidelity of ChebNet The ChebNet encoder generates high-fidelity atom-wise latent representations ($Z^{(t)}$) directly from input conformations. Reconstruction from these unpooled embeddings is excellent (details in Appendix G): for the D2R system ($N = 2191$ atoms), an encoder configuration with a latent dimension $d_z = 16$ achieves a backbone MSE (MSE_{bb}) of 0.0008 and dihedral JSDs around 0.00016. This high-dimensional $Z^{(t)}$ (up to $2191 \times 16 = 35,056$ dimensions in this case) establishes a strong upper benchmark for the atomic detail initially captured. For efficient downstream diffusion modeling, these rich $Z^{(t)}$ embeddings are significantly compressed via a pooling step (Section 3.3) into a much more compact latent vector, \mathbf{h}_0 . This pooling focuses the learning process on conformational *deformations* relative to a reference structure (X_{ref} , provided to the decoder via Z_{ref}), rather than encoding the entire static fold. While this necessary compression means the final generative pipeline’s coordinate accuracy may not fully match the encoder’s standalone reconstruction capabilities, the high intrinsic fidelity of the initial $Z^{(t)}$ ensures that \mathbf{h}_0 is distilled from a robust, deformation-rich representation.

Decoder Reconstruction Fidelity We next assessed decoder reconstruction of all-atom coordinates from these ground-truth ChebNet latents ($Z^{(t)}$), isolating decoder-specific errors (Table 1). The **blind pooling** decoder (using $d_z = 16$ atom features) achieved good coordinate accuracy (IDDT_{All} 0.714) but had limited dihedral precision, evidenced by a blurred Ramachandran plot (visualizing backbone ϕ, ψ angles) and smoothed χ -angle distributions ($\sum \text{JSD}_{\text{sc}}$ 0.0290; Figure 2a, orange traces/distributions). Optional dihedral fine-tuning yielded minimal JSD improvement while slightly reducing IDDTs. In contrast, **sequential pooling** (from $d_z = 8$ atom features) yielded excellent coordinate accuracy (IDDT_{All} 0.718) and superior backbone geometry, marked by sharp Ramachandran plots (Figure 2b, orange trace) and the lowest backbone dihedral divergence ($\sum \text{JSD}_{\text{bb}}$ 0.0026). Its sidechain χ -angle distributions were also well-reproduced ($\sum \text{JSD}_{\text{sc}}$ 0.0192; Figure 2b, orange distributions). Intriguingly, **residue pooling** (from $d_z = 4$ atom features) excelled locally, achieving the lowest backbone/sidechain MSEs (0.083/0.2257) and the best sidechain distributional fidelity ($\sum \text{JSD}_{\text{sc}} = 0.0125$) with outstanding χ -angle reproduction (Figure 2c, orange distributions). This local strength, despite a broader global backbone dihedral distribution ($\sum \text{JSD}_{\text{bb}}$ 0.0078) and a “hazier” Ramachandran plot (Figure 2c, orange trace) partly due to its smaller per-atom latent dimension, stems from its architecture. Pooling features within each of D2R’s $N_{\text{res}} = 273$ residues into $d_p = 4$ local contexts ($z_{\text{res},j}$) provides the MLP with access to a rich information space (effectively $N_{\text{res}} \times d_p \approx 1.1k$ dimensions describing overall residue deformations), boosting local performance. The quality of this decoder stage is key, as the diffusion model samples the distribution defined by these pooled latent embeddings \mathbf{h}_0 .

Diffusion Generation Quality The ultimate test is the quality of conformational ensembles from the full LD-FPG pipeline (Table 2), where pooling strategies yield distinct ensemble characteristics. **Blind pooling** produces structures with the highest global coordinate accuracy scores (IDDT_{All} 0.719, TM_{All} 0.964). However, this global fidelity, likely impacted by the aggressive compression to its final latent \mathbf{h}_0 , sacrifices finer details: its Ramachandran trace (Figure 2a, green trace) is some-

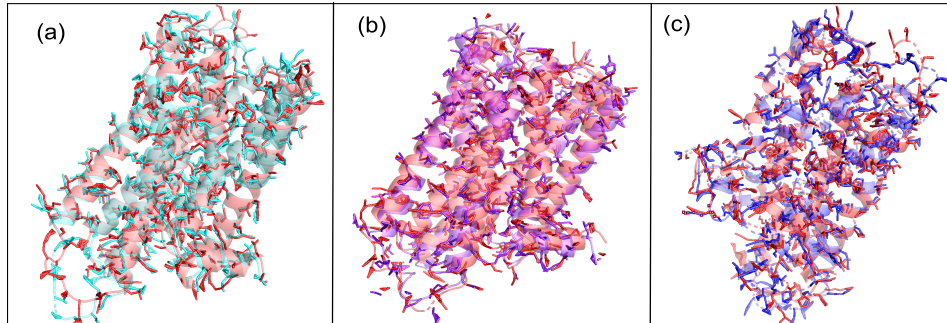


Figure 3: Examples of generated D2R conformations using different pooling strategies. Panels likely correspond to: (a) Blind pooling, (b) sequential pooling, and (c) residue pooling. Structures are visualized to show overall fold and sidechain placement.

what blurred, side-chain distributions are over-smoothed ($\sum \text{JSD}_{\text{sc}}$ 0.04185), and it averages 1350.5 clashes, notably higher than the ≈ 1023 clashes averaged by the ground truth MD ensemble. Rendered structures (Figure 3a) show well-placed helices but wandering χ -angles, leading to protruding or clashing side chains. **Sequential pooling** offers an excellent all-round compromise. It maintains sharp backbone geometry (lowest $\sum \text{JSD}_{\text{bb}}$ 0.0029; clean Ramachandran in Figure 2b, green trace), respectable global scores (IDDT_{All} 0.712), and good side-chain realism ($\sum \text{JSD}_{\text{sc}}$ 0.02895), with an average of 1220.5 clashes. Visually (Figure 3b), models are largely tidy. However, some surface side-chains may still flare out or collide. This aligns with its $\sum \text{JSD}_{\text{sc}}$ being better than blind but not residue pooling, suggesting some χ -angles outside dense rotamer clouds, possibly due to the side-chain decoder’s pooled backbone context leading to ambiguity that diffusion “averages”. Thus, while delivering a sharp backbone and strong side-chain stats, a few rotamers (preferred side-chain conformations) may remain in incorrect basins. Its global backbone statistics are lower after diffusion (IDDT_{All} 0.6880; $\sum \text{JSD}_{\text{bb}}$ 0.0117; Figure 2c, green trace), with occasional backbone kinks (Figure 3c), partly due to its use of a smaller ($d_z = 4$) per-atom latent dimension. However, its per-residue focus excels at χ -angle distributions (best $\sum \text{JSD}_{\text{sc}}$ 0.0224) and yields the lowest average clash count (1145.6, closest to the MD reference), producing the tightest side-chain packing (Figure 3c). In essence, Figure 2 (dihedrals) and Figure 3 (structures) reveal these strategies’ distinct behaviors: blind pooling prioritizes global fold over side-chain details; sequential pooling balances these, with minor outliers; residue pooling excels at rotamers, sometimes with less regular global backbones.

Figure 4 further explores conformational landscape coverage using PCA of latent embeddings and the A100 collective variable, an index of D2R activation states that proxies the MD-sampled landscape. It provides a dual analysis: PCA plots (top row) compare diffusion-generated latent distributions ($\mathbf{h}_0^{\text{gen}}$, red) against MD-derived ones (blue), while A100 value distributions (bottom row) assess the replication of the MD conformational landscape (and its autoencoder/decoder capture) by the full diffusion pipeline. The diffusion models’ ability to cover major PCA regions of the MD latents positively indicates effective learning of the underlying data distribution. When examining the A100 distributions, Blind and Sequential Pooling, operating on more compact, globally-pooled latent spaces (\mathbf{h}_0 with $d_p \approx 100$), show reasonable landscape coverage, with Sequential closely tracing the MD distribution. However, **residue pooling** (Figure 4c, red curve) achieves the most comprehensive A100 landscape capture, populating both primary and subtler MD-observed states often missed by

Table 2: Diffusion Generation Performance.

Model Configuration	IDDT _{All} \uparrow	IDDT _{BB} \uparrow	TM _{All} \uparrow	$\sum \text{JSD}_{\text{bb}}$ \downarrow	$\sum \text{JSD}_{\text{sc}}$ \downarrow	Avg. Clashes \downarrow
Blind pooling	0.719	0.792	0.964	0.006582	0.04185	1350.5
+ Dih. Fine-tuning	0.683	0.748	0.9321	0.00648	0.0409	1340.9
Sequential pooling	0.712	0.801	0.942	0.0029	0.02895	1220.5
Residue pooling	0.6880	0.7575	0.9570	0.0117	0.0224	1145.6

other methods. This superior recovery, despite moderate global backbone metrics, stems from its distinct latent space configuration. Unlike the compact, global latents of Blind/Sequential strategies, residue pooling’s diffusion model leverages a significantly larger effective latent space formed by all per-residue contexts ($N_{\text{res}} \times d_p \approx 1.1k$ for D2R with $d_p = 4$). This richer, structured space, even if derived from a smaller $d_z = 4$ per-atom encoding, enables more nuanced representation of conformational substates. Its proficiency in local rotamer modeling is likely a key contributor, as accurate side-chain placement is crucial for the subtle cooperative shifts defining A100. The decoder’s A100 distribution for residue pooling (Figure 4c, green curve) already indicates robust MD landscape coverage, which the diffusion model effectively samples. Visualizations for residue pooling in Figure 4 employed multi-epoch sampling—aggregating samples from checkpoints across different DDPM training stages, Appendix H.

Furthermore, BioEmu [22], a general MD model, struggled to capture the D2R-specific conformational landscape: its generated A100 distributions (mean -17.19 ± 7.45) markedly diverged from our D2R-MD reference (mean $\approx -47.5 \pm 2.26$), highlighting limitations of such generalist approaches for specific membrane protein ensembles.

5 Conclusion and Future Work

We introduced LD-FPG, a latent diffusion framework generating all-atom protein conformational ensembles from MD data, demonstrated on D2R GPCR. It captures system-specific dynamics, including side-chain details, via learned deformations from a reference. Blind pooling offered global fidelity but compromised side-chain detail and clashes. Sequential pooling provided a strong balance, especially for backbone geometry. Residue pooling excelled in local side-chain accuracy and landscape coverage, despite some global backbone trade-offs and needing multi-epoch sampling for full diversity. A common challenge was increased steric clashes in generated structures versus MD.

Future work includes targeted enhancements. For **Blind and Sequential pooling**, exploring larger pooled latent dimensions (d_p) is immediate, potentially improving detail capture but needing more extensive, diverse training data (e.g., from multiple related protein systems). For **Residue pooling**, with its promising high-dimensional effective latent space ($N_{\text{res}} \times d_p$), better denoisers are key to overcome multi-epoch sampling limits. This might use complex MLP/convolutional architectures, attention for its structured latent vector, or alternative generative models (score-based, flow-matching). For **Sequential pooling**, improving denoiser coverage of the MD-derived latent space (Fig.4b, backbone/sidechain overlap) could resolve side-chain misplacements and boost performance. Broader initiatives will enhance physical realism and architectural sophistication by incorporating lightweight energy surrogates, physics-guided diffusion schemes [60, 61, 28], and advanced architectures like attention-based fusion mechanisms [62–64], SE(3)-equivariant

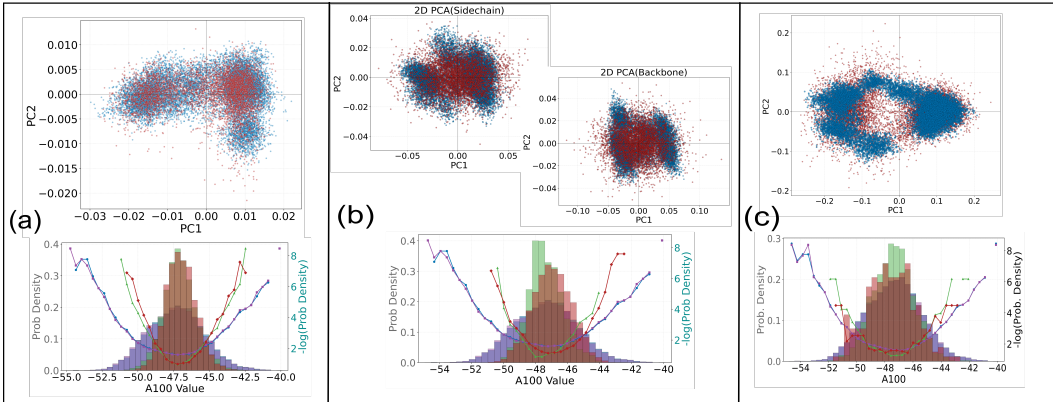


Figure 4: Latent space and collective variable (A100) analysis for Blind (a), Sequential (b), and Residue (c) pooling. Top rows: 2D PCA of dataset (blue) vs. diffusion-generated (red) pooled embeddings (Sequential shows separate backbone/sidechain PCAs). Bottom rows: A100 Value distributions (histograms) and PMFs ($-\log(\text{Probability Density})$) for dataset: ground truth (blue), autoencoder (purple), decoder (green), and generated ensembles (red).

GNNs/transformers, or flow-matching generators [48, 65]. A long-term goal is generalizing LD-FPG by training on data from multiple related proteins (e.g., Class A GPCRs in various states) for foundational models akin to specialized “LLMs for protein dynamics.” Efforts will also cover tailoring pooling for applications, scaling to larger systems [18], and rigorous benchmarking.

Societal Impact: LD-FPG can offer benefits by accelerating drug discovery, improving biological understanding, and enabling protein engineering for medicine/biotechnology. Ethical issues include dual-use, equitable access, data privacy for sensitive data, and rigorous validation to prevent misdirected efforts. Responsible development and ethical dialogue are crucial to maximize benefits and mitigate risks.

References

- [1] Martin Karplus and John Kuriyan. Molecular dynamics and protein function. *Proceedings of the National Academy of Sciences*, 102(19):6679–6685, 2005.
- [2] Katherine Henzler-Wildman and Dorothee Kern. Dynamic personalities of proteins. *Nature*, 450(7172):964–972, 2007.
- [3] John Jumper, Richard Evans, Alexander Pritzel, Tim Green, Michael Figurnov, Olaf Ronneberger, Kathryn Tunyasuvunakool, Russ Bates, Augustin Žídek, Anna Potapenko, et al. Highly accurate protein structure prediction with AlphaFold. *Nature*, 596(7873):583–589, 2021.
- [4] Minkyung Baek, Frank DiMaio, Ivan Anishchenko, Justas Dauparas, Sergey Ovchinnikov, Gyu Rie Lee, Jue Wang, Qian Cong, Lisa N Kinch, R Dustin Schaeffer, et al. Accurate prediction of protein structures and interactions using a three-track neural network. *Science*, 373(6557):871–876, 2021.
- [5] Zeming Lin, Halil Akin, Roshan Rao, Brian Hie, Zhongkai Zhu, Wenting Lu, Nikita Smetanin, Robert Verkuil, Ori Kabeli, Yaniv Shmueli, et al. Evolutionary-scale prediction of atomic-level protein structure with a language model. *Science*, 379(6637):1123–1130, 2023.
- [6] Josh Abramson, Jonas Adler, Jack Dunger, Richard Evans, Tim Green, Alexander Pritzel, Olaf Ronneberger, Lindsay Willmore, Andrew J Ballard, Joshua Bambrick, et al. Accurate structure prediction of biomolecular interactions with alphafold 3. *Nature*, 630(8016):493–500, 2024.
- [7] Jeremy Wohlwend, Gabriele Corso, Saro Passaro, Mateo Reveiz, Ken Leidal, Wojtek Swiderski, Tally Portnoi, Itamar Chinn, Jacob Silterra, Tommi Jaakkola, et al. Boltz-1: Democratizing biomolecular interaction modeling. *bioRxiv*, pages 2024–11, 2024. doi: 10.1101/2024.11.08.622384.
- [8] David D Boehr, Ruth Nussinov, and Peter E Wright. The role of dynamic conformational ensembles in biomolecular recognition. *Nature chemical biology*, 5(11):789–796, 2009.
- [9] Simon J Teague. Implications of protein flexibility for drug discovery. *Nature reviews Drug discovery*, 2(7):527–541, 2003.
- [10] Kuang-Yui Michael Chen, Daniel Keri, and Patrick Barth. Computational design of g protein-coupled receptor allosteric signal transductions. *Nature Chemical Biology*, 16(1):77–86, 2020.
- [11] K-YM Chen, JK Lai, LSP Rudden, J Wang, AM Russell, K Connors, ME Rutter, B Condon, F Tung, L Kodandapani, et al. Computational design of highly signalling-active membrane receptors through solvent-mediated allosteric networks. *Nature Chemistry*, pages 1–10, 2025.
- [12] Rafael Najmanovich, Josef Kuttner, Vladimir Sobolev, and Marvin Edelman. Side-chain flexibility in proteins upon ligand binding. *Proteins: Structure, Function, and Bioinformatics*, 39(3):261–268, 2000.
- [13] Lucas SP Rudden, Mahdi Hijazi, and Patrick Barth. Deep learning approaches for conformational flexibility and switching properties in protein design. *Frontiers in Molecular Biosciences*, 9:928534, 2022.
- [14] Joseph L Watson, David Juergens, Nathaniel R Bennett, Brian L Trippe, Jason Yim, Helen E Eisenach, Woody Ahern, Andrew J Borst, Robert J Ragotte, Lukas F Milles, et al. De novo design of protein structure and function with rfdiffusion. *Nature*, 620(7976):1089–1100, 2023.
- [15] Kevin E Wu, Kevin K Yang, Rianne van den Berg, Sarah Alamdari, James Y Zou, Alex X Lu, and Ava P Amini. Protein structure generation via folding diffusion. *Nature communications*, 15(1):1059, 2024.
- [16] Tomas Geffner, Kieran Didi, Zuobai Zhang, Danny Reidenbach, Zhonglin Cao, Jason Yim, Mario Geiger, Christian Dallago, Emine Kucukbenli, Arash Vahdat, and Karsten Kreis. Proteina: Scaling flow-based protein structure generative models. In *International Conference on Learning Representations (ICLR)*, 2025. OpenReview: TVQLu34bdw.

- [17] Alexander E Chu, Jinho Kim, Lucy Cheng, Gina El Nesr, Minkai Xu, Richard W Shuai, and Po-Ssu Huang. An all-atom protein generative model. *Proceedings of the National Academy of Sciences*, 121(27):e2311500121, 2024.
- [18] John B Ingraham, Max Baranov, Zak Costello, Karl W Barber, Wujie Wang, Ahmed Ismail, Vincent Frappier, Dana M Lord, Christopher Ng-Thow-Hing, Erik R Van Vlack, et al. Illuminating protein space with a programmable generative model. *Nature*, 623(7989):1070–1078, 2023.
- [19] Bodhi P Vani, Akashnathan Aranganathan, Dedi Wang, and Pratyush Tiwary. Alphafold2-rave: From sequence to boltzmann ranking. *Journal of chemical theory and computation*, 19(14):4351–4354, 2023.
- [20] Jiarui Lu, Bozitao Zhong, Zuobai Zhang, and Jian Tang. Str2str: A score-based framework for zero-shot protein conformation sampling. *arXiv preprint arXiv:2306.03117*, 2023.
- [21] Bowen Jing, Bonnie Berger, and Tommi Jaakkola. Alphafold meets flow matching for generating protein ensembles. *arXiv preprint arXiv:2402.04845*, 2024.
- [22] Sarah Lewis, Tim Hempel, José Jiménez-Luna, Michael Gastegger, Yu Xie, Andrew Y. K. Foong, Victor Garcia Satorras, Osama Abdin, Bastiaan S. Veeling, et al. Scalable emulation of protein equilibrium ensembles with generative deep learning. *bioRxiv*, Dec 2024. doi: 10.1101/2024.12.05.626885. preprint.
- [23] Shuxin Zheng, Jiyan He, Chang Liu, Yu Shi, Ziheng Lu, Weitao Feng, Fusong Ju, Jiayi Wang, Jianwei Zhu, Yaosen Min, et al. Predicting equilibrium distributions for molecular systems with deep learning. *Nature Machine Intelligence*, 6(5):558–567, 2024.
- [24] Cong Fu, Keqiang Yan, Limei Wang, Wing Yee Au, Michael Curtis McThrow, Tao Komikado, Koji Maruhashi, Kanji Uchino, Xiaoning Qian, and Shuiwang Ji. A latent diffusion model for protein structure generation. In *Learning on Graphs Conference*, pages 29–1. PMLR, 2024.
- [25] Amy X. Lu, Wilson Yan, Vladimir Gligorijevic, Kyunghyun Cho, Richard Bonneau, Kevin K. Yang, Pieter Abbeel, and Nathan C. Frey. Generating all-atom protein structure from sequence-only training data. *bioRxiv preprint*, 2024. doi: 10.1101/2024.12.19.630448. doi: 10.1101/2024.12.19.630448.
- [26] Giacomo Janson and Michael Feig. Transferable deep generative modeling of intrinsically disordered protein conformations. *PLoS Computational Biology*, 20(5):e1012144, 2024.
- [27] Yan Wang, Lihao Wang, Yuning Shen, Yiqun Wang, Huizhuo Yuan, Yue Wu, and Quanquan Gu. Protein conformation generation via force-guided SE(3) diffusion models. In *Proceedings of the 41st International Conference on Machine Learning*, volume 235 of *Proceedings of Machine Learning Research*, pages 56835–56859, 2024. URL <https://proceedings.mlr.press/v235/wang24cv.html>. arXiv:2403.14088.
- [28] Yikai Liu, Abhilash Sahoo, Zongxin Yu, Guang Lin, Ming Chen, and Sonya M. Hanson. EGDiff: An experiment-guided diffusion model for protein conformational ensemble generation. *bioRxiv preprint*, 2024. doi: 10.1101/2024.10.04.616517. version 1 posted Oct 4 2024.
- [29] Naomi R. Latorraca, A. J. Venkatakrishnan, and Ron O. Dror. GPCR dynamics: Structures in motion. *Chemical Reviews*, 117(1):139–155, 2017.
- [30] Mingyang Zhang, Ting Chen, Xun Lu, Xiaobing Lan, Ziqiang Chen, and Shaoyong Lu. G protein-coupled receptors (gpcrs): advances in structures, mechanisms and drug discovery. *Signal Transduction and Targeted Therapy*, 9(1), 2024. ISSN 2059-3635. doi: 10.1038/s41392-024-01803-6. URL <http://dx.doi.org/10.1038/s41392-024-01803-6>.
- [31] Vicent Casadó and Verònica Casadó-Anguera. What are the current trends in g protein-coupled receptor targeted drug discovery? *Expert Opinion on Drug Discovery*, 18(8):815–820, 2023. ISSN 1746-045X. doi: 10.1080/17460441.2023.2216014. URL <http://dx.doi.org/10.1080/17460441.2023.2216014>.

- [32] Dehua Yang, Qingtong Zhou, Viktorija Labroska, Shanshan Qin, Sanaz Darbalaei, Yiran Wu, Elita Yuliantie, Linshan Xie, Houchao Tao, Jianjun Cheng, Qing Liu, Suwen Zhao, Wenqing Shui, Yi Jiang, and Ming-Wei Wang. G protein-coupled receptors: structure- and function-based drug discovery. *Signal Transduction and Targeted Therapy*, 6(1), 2021. ISSN 2059-3635. doi: 10.1038/s41392-020-00435-w. URL <http://dx.doi.org/10.1038/s41392-020-00435-w>.
- [33] David S Wishart, Yannick D Feunang, An C Guo, Elvis J Lo, Ana Marcu, Jason R Grant, Tanvir Sajed, Daniel Johnson, Carin Li, Zinat Sayeeda, et al. Drugbank 5.0: a major update to the drugbank database for 2018. *Nucleic acids research*, 46(D1):D1074–D1082, 2018.
- [34] Daniel Hilger, Matthieu Masureel, and Brian K Kobilka. Structure and dynamics of gpcr signaling complexes. *Nature structural & molecular biology*, 25(1):4–12, 2018.
- [35] J. Monod, J. Wyman, and J.-P. Changeux. On the nature of allosteric transitions: A plausible model. *Journal of Molecular Biology*, 12(1):88–118, 1965.
- [36] Naomi R Latorraca, AJ Venkatakrishnan, and Ron O Dror. Gpcr dynamics: structures in motion. *Chemical reviews*, 117(1):139–155, 2017.
- [37] Robert E Jefferson, Aurélien Oggier, Andreas Füglistaler, Nicolas Camviel, Mahdi Hijazi, Ana Rico Villarreal, Caroline Arber, and Patrick Barth. Computational design of dynamic receptor—peptide signaling complexes applied to chemotaxis. *Nature Communications*, 14(1):2875, 2023.
- [38] Terry Kenakin. Biased receptor signaling in drug discovery. *Pharmacological reviews*, 71(2):267–315, 2019.
- [39] E. Goupil, S. A. Laporte, and T. E. Hebert. Functional selectivity in gpcr signaling: Understanding the full spectrum of receptor conformations. *Mini-Reviews in Medicinal Chemistry*, 12(9):817–830, 2012. ISSN 1389-5575. doi: 10.2174/138955712800959143. URL <http://dx.doi.org/10.2174/138955712800959143>.
- [40] P. Jeffrey Conn, Arthur Christopoulos, and Craig W. Lindsley. Allosteric modulators of gpcrs: a novel approach for the treatment of cns disorders. *Nature Reviews Drug Discovery*, 8(1):41–54, 2009. ISSN 1474-1784. doi: 10.1038/nrd2760. URL <http://dx.doi.org/10.1038/nrd2760>.
- [41] Hung N Do, Jinan Wang, and Yinglong Miao. Deep learning dynamic allostery of G-Protein-Coupled receptors. *JACS Au*, 3(11):3165–3180, 2023.
- [42] Jon Kapla, Ismael Rodríguez-Espigares, Flavio Ballante, Jana Selent, and Jens Carlsson. Can molecular dynamics simulations improve the structural accuracy and virtual screening performance of gpcr models? *PLOS Computational Biology*, 17(5):e1008936, 2021. ISSN 1553-7358. doi: 10.1371/journal.pcbi.1008936. URL <http://dx.doi.org/10.1371/journal.pcbi.1008936>.
- [43] Xin-heng He, Chong-zhao You, Hua-liang Jiang, Yi Jiang, H. Eric Xu, and Xi Cheng. Alphafold2 versus experimental structures: evaluation on g protein-coupled receptors. *Acta Pharmacologica Sinica*, 44(1):1–7, 2022. ISSN 1745-7254. doi: 10.1038/s41401-022-00938-y. URL <http://dx.doi.org/10.1038/s41401-022-00938-y>.
- [44] Ismael Rodríguez-Espigares, Mariona Torrens-Fontanals, Johanna KS Tiemann, David Aranda-García, Juan Manuel Ramírez-Angueta, Tomasz Maciej Stepniewski, Nathalie Worp, Alejandro Varela-Rial, Adrián Morales-Pastor, Brian Medel-Lacruz, et al. Gpcrmd uncovers the dynamics of the 3d-gpcr. *Nature Methods*, 17(8):777–787, 2020.
- [45] J M López-Correa, C König, and A Vellido. Gpcr molecular dynamics forecasting using recurrent neural networks. *Scientific Reports*, 14(1):9942, 2024. doi: 10.1038/s41598-023-48346-4.
- [46] Michaël Defferrard, Xavier Bresson, and Pierre Vandergheynst. Convolutional neural networks on graphs with fast localized spectral filtering. *Advances in neural information processing systems*, 29, 2016.

- [47] Jonathan Ho, Ajay Jain, and Pieter Abbeel. Denoising diffusion probabilistic models. In *Advances in Neural Information Processing Systems*, volume 33, pages 6840–6851, 2020.
- [48] Yaron Lipman, Ricky TQ Chen, Heli Ben-Hamu, Maximilian Nickel, and Matt Le. Flow matching for generative modeling. *arXiv preprint arXiv:2210.02747*, 2022.
- [49] Guillaume Huguet, James Vuckovic, Kilian Fatras, Eric Thibodeau-Laufer, Pablo Lemos, Rishat Islam, Cheng-Hao Liu, Jarrid Rector-Brooks, Tara Akhound-Sadegh, Michael Bronstein, et al. Sequence-augmented se (3)-flow matching for conditional protein backbone generation. *arXiv preprint arXiv:2405.20313*, 2024.
- [50] Raphael R Eguchi, Christian A Choe, and Po-Ssu Huang. Ig-vae: Generative modeling of protein structure by direct 3d coordinate generation. *PLoS computational biology*, 18(6): e1010271, 2022.
- [51] Jin Sub Lee and Philip M Kim. FlowPacker: Protein side-chain packing with torsional flow matching. *Bioinformatics*, page btaf010, 2025. doi: 10.1093/bioinformatics/btaf010.
- [52] Shiwei Liu, Tian Zhu, Milong Ren, Chungong Yu, Dongbo Bu, and Haicang Zhang. Predicting mutational effects on protein-protein binding via a side-chain diffusion probabilistic model. *Advances in Neural Information Processing Systems*, 36:48994–49005, 2023.
- [53] Sanaa Mansoor, Minkyung Baek, Hahnbeom Park, Gyu Rie Lee, and David Baker. Protein ensemble generation through variational autoencoder latent space sampling. *Journal of Chemical Theory and Computation*, 20(7):2689–2695, 2024.
- [54] Yaowei Jin, Qi Huang, Ziyang Song, Mingyue Zheng, Dan Teng, and Qian Shi. P2dflow: A protein ensemble generative model with SE(3) flow matching. *Journal of Chemical Theory and Computation*, 21(6):3288–3296, 2025. doi: 10.1021/acs.jctc.4c01620.
- [55] Bowen Jing, Bonnie Berger, and Tommi Jaakkola. Generative modeling of molecular dynamics trajectories. *arXiv preprint arXiv:2409.17808*, 2024. NeurIPS 2024 ML4LMS Workshop Poster.
- [56] Wolfgang Kabsch. A solution for the best rotation to relate two sets of vectors. *Acta Crystallographica Section A: Crystal Physics, Diffraction, Theoretical and General Crystallography*, 32(5):922–923, 1976.
- [57] Passainte Ibrahim, David Wifling, and Timothy Clark. Universal activation index for class a gpcrs. *Journal of Chemical Information and Modeling*, 59(9):3938–3945, 2019.
- [58] A Paszke. Pytorch: An imperative style, high-performance deep learning library. *arXiv preprint arXiv:1912.01703*, 2019.
- [59] Diederik P Kingma and Jimmy Ba. Adam: A method for stochastic optimization. *arXiv preprint arXiv:1412.6980*, 2014.
- [60] Yanbin Wang and Ming Chen. Diffpie: Guiding deep generative models to explore protein conformations under external interactions. *bioRxiv*, pages 2025–04, 2025.
- [61] Kexin Zhang, Yuanyuan Ma, Jiale Yu, Huiting Luo, Jinyu Lin, Yifan Qin, Xiangcheng Li, Qian Jiang, Fang Bai, Jiayi Dou, et al. Physdock: A physics-guided all-atom diffusion model for protein-ligand complex prediction. *bioRxiv*, pages 2025–04, 2025.
- [62] Valentin Lombard, Sergei Grudinin, and Elodie Laine. Petimot: A novel framework for inferring protein motions from sparse data using se (3)-equivariant graph neural networks. *arXiv preprint arXiv:2504.02839*, 2025.
- [63] Ada Fang, Zaixi Zhang, Andrew Zhou, and Marinka Zitnik. Atomica: Learning universal representations of intermolecular interactions. *bioRxiv*, pages 2025–04, 2025.
- [64] Chaitanya K Joshi, Xiang Fu, Yi-Lun Liao, Vahe Gharakhanyan, Benjamin Kurt Miller, Anuroop Sriram, and Zachary W Ulissi. All-atom diffusion transformers: Unified generative modelling of molecules and materials. 2025.

- [65] Yangtian Zhan, Zuobai Zhang, Tianfan Li, Yu Tian, Hao Li, Sheng Wang, and Jian Xu. P2DFlow: A protein ensemble generative model with SE(3) flow matching. *arXiv preprint arXiv:2411.17196*, 2024.
- [66] Sheng Wang, Tao Che, Anat Levit, Brian K Shoichet, Daniel Wacker, and Bryan L Roth. Structure of the d2 dopamine receptor bound to the atypical antipsychotic drug risperidone. *Nature*, 555(7695):269–273, 2018.
- [67] Po-Ssu Huang, Yih-En Andrew Ban, Florian Richter, Ingemar Andre, Robert Vernon, William R Schief, and David Baker. Rosettaremodel: a generalized framework for flexible backbone protein design. *PloS one*, 6(8):e24109, 2011.
- [68] Emilia L Wu, Xi Cheng, Sunhwan Jo, Huan Rui, Kevin C Song, Eder M Dávila-Contreras, Yifei Qi, Jumin Lee, Viviana Monje-Galvan, Richard M Venable, et al. Charmm-gui membrane builder toward realistic biological membrane simulations, 2014.
- [69] Pekka Mark and Lennart Nilsson. Structure and dynamics of the tip3p, spc, and spc/e water models at 298 k. *The Journal of Physical Chemistry A*, 105(43):9954–9960, 2001.
- [70] Jing Huang, Sarah Rauscher, Grzegorz Nawrocki, Ting Ran, Michael Feig, Bert L De Groot, Helmut Grubmüller, and Alexander D MacKerell Jr. Charmm36m: an improved force field for folded and intrinsically disordered proteins. *Nature methods*, 14(1):71–73, 2017.
- [71] Mark James Abraham, Teemu Murtola, Roland Schulz, Szilárd Páll, Jeremy C Smith, Berk Hess, and Erik Lindahl. Gromacs: High performance molecular simulations through multi-level parallelism from laptops to supercomputers. *SoftwareX*, 1:19–25, 2015.
- [72] Giovanni Bussi, Davide Donadio, and Michele Parrinello. Canonical sampling through velocity rescaling. *The Journal of chemical physics*, 126(1), 2007.
- [73] Mattia Bernetti and Giovanni Bussi. Pressure control using stochastic cell rescaling. *The Journal of Chemical Physics*, 153(11), 2020.
- [74] Berk Hess, Henk Bekker, Herman JC Berendsen, and Johannes GEM Fraaije. Lincs: A linear constraint solver for molecular simulations. *Journal of computational chemistry*, 18(12):1463–1472, 1997.
- [75] Ulrich Essmann, Lalith Perera, Max L Berkowitz, Tom Darden, Hsing Lee, and Lee G Pedersen. A smooth particle mesh ewald method. *The Journal of chemical physics*, 103(19):8577–8593, 1995.
- [76] Valerio Mariani, Marco Biasini, Alessandro Barbato, and Torsten Schwede. lddt: a local superposition-free score for comparing protein structures and models using distance difference tests. *Bioinformatics*, 29(21):2722–2728, 2013.
- [77] Yang Zhang and Jeffrey Skolnick. Tm-align: a protein structure alignment algorithm based on the tm-score. *Nucleic acids research*, 33(7):2302–2309, 2005.
- [78] Peter JA Cock, Tiago Antao, Jeffrey T Chang, Brad A Chapman, Cymon J Cox, Andrew Dalke, Iddo Friedberg, Thomas Hamelryck, Frank Kauff, Bartek Wilczynski, et al. Biopython: freely available python tools for computational molecular biology and bioinformatics. *Bioinformatics*, 25(11):1422, 2009.
- [79] Pauli Virtanen, Ralf Gommers, Travis E. Oliphant, Matt Haberland, Tyler Reddy, David Cournapeau, Evgeni Burovski, Pearu Peterson, Warren Weckesser, Jonathan Bright, Stéfan J. van der Walt, Matthew Brett, Joshua Wilson, K. Jarrod Millman, Nikolay Mayorov, Andrew R. J. Nelson, Eric Jones, Robert Kern, Eric Larson, C J Carey, İlhan Polat, Yu Feng, Eric W. Moore, Jake VanderPlas, Denis Laxalde, Josef Perktold, Robert Cimrman, Ian Henriksen, E. A. Quintero, Charles R. Harris, Anne M. Archibald, Antônio H. Ribeiro, Fabian Pedregosa, Paul van Mulbregt, and SciPy 1.0 Contributors. SciPy 1.0: Fundamental Algorithms for Scientific Computing in Python. *Nature Methods*, 17:261–272, 2020. doi: 10.1038/s41592-019-0686-2.

- [80] Yurui Qian, Qi Cai, Yingwei Pan, Yehao Li, Ting Yao, Qibin Sun, and Tao Mei. Boosting diffusion models with moving average sampling in frequency domain. In *Proceedings of the IEEE/CVF Conference on Computer Vision and Pattern Recognition*, pages 8911–8920, 2024.
- [81] Peter Henderson, Jieru Hu, Joshua Romoff, Emma Brunskill, Dan Jurafsky, and Joelle Pineau. Towards the systematic reporting of the energy and carbon footprints of machine learning. *Journal of Machine Learning Research*, 21(248):1–43, 2020.
- [82] <https://www.nvidia.com/en-us/data-center/l40s/>.
- [83] <https://www.hyperstack.cloud/technical-resources/performance-benchmarks/comparing-nvidia-h100-pcie-vs-sxm-performance-use-cases-and-more>.
- [84] <https://journal.uptimeinstitute.com/large-data-centers-are-mostly-more-efficient-analysis-confirms/>.
- [85] <https://ember-energy.org/chapter/electricity-transition-in-2022-ger2023/>.
- [86] <https://aliunid.com/wp-content/uploads/2023/04/2023-media-information-aliunid-CO2-content-in-Swiss-electricity.pdf>.

A Methodology Overview and Notation

This section provides a consolidated overview of the LD-FPG framework’s workflow, key mathematical notation used throughout the paper, and supplementary details regarding data processing, model architectures, and training procedures.

A.1 Notation

We define the following notation used throughout the main text and appendix:

- k : Number of nearest neighbors used for graph construction.
- $\tilde{X}^{(t)} \in \mathbb{R}^{N \times 3}$: Raw (unaligned) Molecular Dynamics coordinates for frame t .
- Θ : Encoder neural network function; Θ^* denotes frozen, pre-trained encoder parameters.
- K : Order of Chebyshev polynomials in the ChebNet encoder.
- d_c : Dimensionality of the conditioner tensor C .
- H, W : Output dimensions (height and width respectively) for pooling layers, where $d_p = H \cdot W$.
- N_{layers} : Number of layers in a Multi-Layer Perceptron (MLP).
- $\mathcal{L}_{\text{diffusion}}$: Loss function for training the Denoising Diffusion Probabilistic Model (DDPM).
- N : Total heavy atoms per structure.
- $V = \{1, \dots, N\}$: Atom nodes.
- $G = (V, E)$: Graph representation.
- $\mathcal{I}_{\text{bb}} \subset V$: Backbone atom indices; $N_{\text{bb}} = |\mathcal{I}_{\text{bb}}|$.
- $\mathcal{I}_{\text{sc}} \subset V$: Sidechain atom indices; $N_{\text{sc}} = |\mathcal{I}_{\text{sc}}|$. ($V = \mathcal{I}_{\text{bb}} \cup \mathcal{I}_{\text{sc}}$).
- $z_{\text{res},j} \in \mathbb{R}^{d_p}$: Local pooled context vector summarizing the deformation of residue R_j (this corresponds to $\mathbf{h}_{R_j}^{(b)}$ as used in Appendix C.3).
- $X_{\text{true}} \in \mathbb{R}^{N \times 3}$: Ground truth aligned coordinates. $X_{\text{true}}^{(b,i)}$ for atom i , sample b .
- $X_{\text{pred}} \in \mathbb{R}^{N \times 3}$: Predicted coordinates.
- $X_{\text{ref}} \in \mathbb{R}^{N \times 3}$: Reference structure coordinates (e.g., first frame).
- d_z : Encoder latent embedding dimensionality.
- $Z \in \mathbb{R}^{N \times d_z}$: Latent atom embeddings from encoder: $Z = \text{Encoder}(X_{\text{true}}, E)$.
- $Z_{\text{ref}} \in \mathbb{R}^{N \times d_z}$: Reference structure latent embeddings: $Z_{\text{ref}} = \text{Encoder}(X_{\text{ref}}, E_{\text{ref}})$.
- $C \in \mathbb{R}^{N \times d_c}$: General conditioning tensor (typically $C = Z_{\text{ref}}$). C_{ex} is batch-expanded.
- d_p : Pooled context vector dimension.
- \mathcal{P} : Generic pooling operator.
- $\mathcal{R} = \{R_1, \dots, R_{N_{\text{res}}}\}$: Partition of atoms into residues.
- $f: V \rightarrow \{1, \dots, N_{\text{res}}\}$: Atom-to-residue mapping.
- ϕ, ψ, χ_k : Dihedral angles; $\alpha \in \mathcal{A}$ is a generic type.
- $M_\alpha(j)$: Mask for valid angle α in residue j .
- $P(\alpha_{\text{pred}}), P(\alpha_{\text{true}})$: Empirical angle distributions.
- $D(\cdot \| \cdot)$: Divergence function (KL, JS).
- $w_{\text{base}}, \lambda_{\text{mse}}, \lambda_{\text{div}}$: Loss weights.
- f_{dih} : Probability of applying dihedral-based loss terms during stochastic fine-tuning.
- $\|\mathbf{v}\|^2$: Squared Euclidean norm.
- T : Diffusion timesteps.
- $\beta_t, \alpha_t, \bar{\alpha}_t$: Diffusion schedule parameters.

- \mathbf{h}_0 : Initial pooled latent embedding for diffusion.
- \mathbf{h}_t : Noisy latent at step t .
- $\epsilon \sim \mathcal{N}(0, I)$: Standard Gaussian noise.
- $\epsilon_\theta(\mathbf{h}_t, t)$: Denoising network predicting noise ϵ .

A.2 Overall Training and Generation Workflow

The LD-FPG framework follows a multi-phase training and generation procedure, outlined in Algorithm 1.

Algorithm 1 Overall Training and Generation Workflow (LD-FPG)

```
1: Input: Aligned coordinates file (my_protein.json), Topology file
   (condensed_residues.json), Reference PDB (heavy_chain.pdb).
2: Parameters: Encoder config ( $d_z, K, \dots$ ), Decoder config (Pooling Type,  $H, W, N_{layers}, \dots$ ),
   Optional fine-tuning weights ( $\lambda_{mse}, \lambda_{div}$ ), Diffusion config ( $T, \beta_{start}, \beta_{end}, \epsilon_\theta$  type).
   // — Preprocessing (Details in Appendix B) —
3: Load aligned coordinates  $\{X_{true}^{(f)}\}_{f=1}^{N_{frames}}$  from my_protein.json.
4: Load topology (atom indices  $\mathcal{I}_{bb}, \mathcal{I}_{sc}$ , residue map  $f$ , dihedral defs.) from
   condensed_residues.json.
5: Build graph dataset  $GraphDataset = \{\text{BuildGraph}(X_{true}^{(f)}, k=4)\}_{f=1}^{N_{frames}}$ .
   // — Phase 1: Encoder Pre-training (Optional) (Details in Appendix I.3) —
6: Initialize Encoder $_\theta$  (ChebNet model).
7: Train Encoder $_\theta$  on  $GraphDataset$  using coordinate reconstruction loss  $\mathcal{L}_{HNO}$  (Eq. in Ap-
   pendix E).
8: Save best encoder parameters  $\theta^*$ .
   // — Phase 2: Decoder Training (Details in Appendix C) —
9: Load pre-trained Encoder $_{\theta^*}$  and freeze weights.
10: Generate latent embeddings  $Z^{(f)} = \text{Encoder}_{\theta^*}(X_{true}^{(f)})$  for all frames  $f$ .
11: Create Decoder Input Dataset  $D_{dec} = \{(Z^{(f)}, X_{true}^{(f)}) \mid f = 1..N_{frames}\}$ .
12: Define conditioner  $C = Z_{ref} = \text{Encoder}_{\theta^*}(X_{true}^{(1)})$  (Details in Appendix I.9).
13: Select Decoder Variation:
14: if PoolingType is Blind then
15:   Initialize Decoder $_\phi \leftarrow \text{BlindPoolingDecoder}(\dots)$ .
16:   Train Decoder $_\phi$  on  $D_{dec}$  using coordinate loss  $\mathcal{L}_{Dec} = \mathcal{L}_{coord}$ .
17:   Optional Fine-tuning: Continue training with  $\mathcal{L}_{Dec} = w_{base}\mathcal{L}_{coord} + \lambda_{mse}\mathcal{L}_{mse\_dih} +$ 
      $\lambda_{div}\mathcal{L}_{div\_dih}$  (stochastically, see Appendix E).
18:   Save best decoder parameters  $\phi^*$ .
19: else if PoolingType is Sequential then
20:   Initialize BBDecoder $_{\phi_{bb}}, \text{SCDecoder}_{\phi_{sc}}(\dots)$ .
21:   Train BBDecoder $_{\phi_{bb}}$  on  $D_{dec}$  using  $\mathcal{L}_{BB} = \mathcal{L}_{coord}^{bb}$ . Freeze  $\phi_{bb}^*$ .
22:   Train SCDecoder $_{\phi_{sc}}$  on  $D_{dec}$  using  $\mathcal{L}_{SC} = \mathcal{L}_{coord}^{full}$  (requires frozen BBDecoder $_{\phi_{bb}^*}$ ).
23:   Save best parameters  $\phi_{bb}^*, \phi_{sc}^*$ .
24: else if PoolingType is Residue-Based then
25:   Initialize Decoder $_\phi \leftarrow \text{ResidueBasedDecoder}(\dots)$ .
26:   Train Decoder $_\phi$  on  $D_{dec}$  using coordinate loss  $\mathcal{L}_{Dec} = \mathcal{L}_{coord}$ .
27:   Save best decoder parameters  $\phi^*$ .
28: end if
   // — Phase 3: Latent Diffusion Training (Details in Appendix D) —
29: Load best Encoder $_{\theta^*}$  and Decoder $_{\phi^*}$  (or relevant pooling part).
30: Generate pooled latent embeddings  $\mathbf{h}_0^{(f)} = \text{Pool}(Z^{(f)})$  for all  $f$ , using the specific pooling
   mechanism of the chosen decoder.
31: Create  $DiffusionInputDataset = \{\mathbf{h}_0^{(f)}\}$ .
32: Initialize  $\epsilon_\theta$  (Denoising model).
33: Train  $\epsilon_\theta$  on  $DiffusionInputDataset$  using  $\mathcal{L}_{diffusion}$  (Eq. 2).
34: Save best diffusion model parameters  $\theta_{diff}^*$ .
   // — Output Generation (Sampling) —
35: Load best models: Encoder $_{\theta^*}$ , Decoder $_{\phi^*}$  (or BBDecoder $_{\phi_{bb}^*}, \text{SCDecoder}_{\phi_{sc}^*}$ ),  $\epsilon_{\theta_{diff}}^*$ .
36: Sample novel pooled latent(s)  $\mathbf{h}_0^{gen}$  using  $\epsilon_{\theta_{diff}}^*$  (Algorithm in Appendix D).
37: Decode generated latent(s): (Feed  $\mathbf{h}_0^{gen}$  into appropriate decoder stage)
38:  $X_{pred}^{gen} \leftarrow \text{Decoder}_{\phi^*}(\dots, \text{context} = \mathbf{h}_0^{gen}, C)$ 
39: Output: Generated coordinates  $\{X_{pred}^{gen}\}$ 
```

B Input Data Processing and Representation

The raw Molecular Dynamics (MD) simulation data (trajectory processing detailed in Appendix F.1) is transformed into a structured format suitable for the machine learning pipeline. This involves generating two key JSON files using custom Python scripts (see Supplementary Code for `extract_residues.py` and `condense_json.py`): one defining the static topology of the protein with a consistent indexing scheme (`condensed_residues.json`), and another containing per-frame coordinate and dihedral angle data.

B.1 Static Topology and Consistent Indexing File (`condensed_residues.json`)

To provide a consistent structural map for the machine learning models, a static JSON file, typically named `condensed_residues.json`, is generated. This file is crucial as it establishes a definitive and model-centric representation of the protein’s topology:

- **Zero-Based Contiguous Atom Indexing:** A new, zero-based, and contiguous indexing scheme ($0, 1, \dots, N - 1$) is created for all N heavy atoms in the protein system. This re-indexing maps original PDB atom identifiers to a consistent integer range, essential for constructing graph inputs and feature matrices for the neural network.
- **Residue Definitions:** Residues are also re-indexed contiguously (e.g., $0, \dots, N_{\text{res}} - 1$). For each re-indexed residue, the file stores:
 - The residue type (e.g., 'ALA', 'LYS').
 - Lists of atom indices (using the *new zero-based scheme*) that constitute the backbone atoms of that residue.
 - Lists of atom indices (using the *new zero-based scheme*) that constitute the sidechain heavy atoms of that residue.
- **Dihedral Angle Definitions (Atom Quadruplets):** This is a critical component for calculating dihedral-based losses and analyses. For each residue, the file stores definitions for all applicable standard backbone angles (ϕ, ψ) and sidechain angles ($\chi_1, \chi_2, \chi_3, \chi_4, \chi_5$). Each dihedral angle is defined by an ordered quadruplet of four atom indices. Crucially, these atom indices adhere to the *new, zero-based, contiguous indexing scheme*. For example, a ϕ angle for a specific residue would be defined by four specific integer indices from the $0 \dots N - 1$ range. This allows for unambiguous calculation of any dihedral angle directly from a set of N atomic coordinates, whether they are ground truth or model-predicted. The definitions also account for residue types where certain χ angles are not present (e.g., Alanine has no χ angles, Glycine has no sidechain).

B.2 Primary Per-Frame Data File

This second JSON file stores the dynamic information extracted from each frame of the MD trajectory. For every snapshot:

- **Heavy Atom Coordinates:** The 3D Cartesian coordinates of all heavy atoms are recorded after rigid-body alignment to a common reference frame (the first frame of the trajectory, as described in Section 3.1). These coordinates are stored in an order that corresponds to the new zero-based indexing defined in the static topology file.
- **Dihedral Angle Values:** The values for standard backbone dihedral angles (ϕ, ψ) and sidechain dihedral angles (χ_1 through χ_5 , where applicable for each residue type) are pre-calculated. These calculations initially use atom identifications based on the original PDB residue and atom naming conventions but are stored in a way that can be mapped to the new indexing if needed for direct comparison or analysis.

This primary data file is typically organized on a per-residue basis (using original PDB residue numbering for initial organization if helpful during generation), associating each residue with its constituent atoms’ names, original PDB indices, and the time series of their coordinates and calculated dihedral angles.

B.3 Usage in Models

The two JSON files are used in conjunction:

- The static topology file (`condensed_residues.json`) serves as the definitive reference for all structural metadata used by the model during training and inference. This includes identifying which atoms belong to the backbone versus sidechain (using their new zero-based indices) and, most importantly, providing the specific quadruplets of new zero-based atom indices required to calculate any dihedral angle from a given set of 3D coordinates. This capability is essential for implementing the dihedral angle-based loss terms ($\mathcal{L}_{\text{mse_dih}}$, $\mathcal{L}_{\text{div_dih}}$) mentioned in Section 3.5, as these losses operate on dihedral angles computed from the model’s predicted coordinates (X_{pred}).
- The 3D coordinates for each heavy atom, required as input features ($X^{(t)}$) for the encoder at each frame t , are drawn from the primary per-frame data file. These coordinates must be arranged and ordered according to the *new zero-based indexing scheme* established by the static topology file to ensure consistency with the model’s internal graph representation.

This separation of dynamic coordinate data from static, re-indexed topological information allows for efficient data loading and consistent geometric calculations within the LD-FPG framework.

C Decoder Architectures and Pooling Strategies

This section provides a detailed description of the three primary pooling strategies employed within the decoder architectures: Blind pooling, sequential pooling, and residue-based pooling. For each strategy, we delineate how atom-wise latent embeddings $Z \in \mathbb{R}^{B \times N \times d_z}$ (where B is batch size, N is the number of heavy atoms, and d_z is the latent dimension per atom) and a conditioner $C \in \mathbb{R}^{N \times d_c}$ (typically the latent representation of the reference structure, Z_{ref}) are processed to generate the input for the final coordinate prediction MLP. Specific hyperparameter configurations for representative models are detailed in the Extended Technical Appendix (Section I).

C.1 Blind Pooling Strategy

The blind pooling strategy aims to capture a global context from all atom embeddings for the entire protein structure. Let $Z^{(b)} \in \mathbb{R}^{N \times d_z}$ be the latent atom embeddings for a single sample b in a batch.

1. **Global Pooling:** The atom embeddings $Z^{(b)}$ are treated as an image-like tensor and processed by a 2D adaptive average pooling layer, $\mathcal{P}_{\text{global}}$ (typically `nn.AdaptiveAvgPool2d` with output size $H \times W$). This operation pools across all N atoms for each sample in the batch:

$$\mathbf{h}_{\text{global}}^{(b)} = \mathcal{P}_{\text{global}}(Z^{(b)}) \in \mathbb{R}^{d_p}$$

where $d_p = H \cdot W$ is the dimension of the pooled global context vector. For a batch, this results in $\mathbf{H}_{\text{global}} \in \mathbb{R}^{B \times d_p}$.

2. **Context Expansion:** This global context vector $\mathbf{h}_{\text{global}}^{(b)}$ is then expanded (tiled) to match the number of atoms N , resulting in $\mathbf{H}_{\text{global.ex}}^{(b)} \in \mathbb{R}^{N \times d_p}$, where each row i (for atom i) is identical to $\mathbf{h}_{\text{global}}^{(b)}$. For a batch, this is $\mathbf{H}_{\text{global.ex}} \in \mathbb{R}^{B \times N \times d_p}$.
3. **Conditioner Expansion:** The conditioner $C \in \mathbb{R}^{N \times d_c}$ is expanded for the batch to $C_{\text{ex}} \in \mathbb{R}^{B \times N \times d_c}$.
4. **MLP Input Formulation:** For each atom i in sample b , the input to the final MLP, M_{blind} , is formed by concatenating its corresponding expanded global context and its conditioner vector:

$$M_{\text{in}}^{(b,i)} = \text{concat}(\mathbf{h}_{\text{global}}^{(b)}, C^{(b,i)}) \in \mathbb{R}^{d_p+d_c}$$

Note that $\mathbf{h}_{\text{global}}^{(b)}$ is the same for all atoms i within sample b .

5. **Coordinate Prediction:** A shared $\text{MLP}_{\text{blind}}$ processes $M_{\text{in}}^{(b,i)}$ for each atom to predict its 3D coordinates:

$$X_{\text{pred}}^{(b,i)} = \text{MLP}_{\text{blind}}(M_{\text{in}}^{(b,i)}) \in \mathbb{R}^3$$

This results in the full predicted structure $X_{\text{pred}} \in \mathbb{R}^{B \times N \times 3}$.

C.2 Sequential Pooling Strategy

The sequential pooling strategy decodes the protein structure in two stages: first the backbone atoms (\mathcal{I}_{bb}), then the sidechain atoms (\mathcal{I}_{sc}), using information from the preceding stage.

C.2.1 Backbone Decoder Stage

Let $Z^{(b)} \in \mathbb{R}^{N \times d_z}$ be the full latent atom embeddings and $C^{(b)} \in \mathbb{R}^{N \times d_c}$ be the full conditioner for sample b .

1. **Backbone Embedding Selection:** Latent embeddings $Z_{\text{bb}}^{(b)} \in \mathbb{R}^{N_{\text{bb}} \times d_z}$ and conditioner vectors $C_{\text{bb}}^{(b)} \in \mathbb{R}^{N_{\text{bb}} \times d_c}$ corresponding to backbone atoms \mathcal{I}_{bb} are selected.
2. **Backbone Pooling:** $Z_{\text{bb}}^{(b)}$ is pooled using a 2D adaptive average pooling layer \mathcal{P}_{bb} (e.g., `BlindPooling2D` from the implementation, with output size $H_{\text{bb}} \times W_{\text{bb}}$) to obtain a backbone-specific context vector:

$$\mathbf{h}_{\text{bb}}^{(b)} = \mathcal{P}_{\text{bb}}(Z_{\text{bb}}^{(b)}) \in \mathbb{R}^{d_{p,\text{bb}}}$$

where $d_{p,\text{bb}} = H_{\text{bb}} \cdot W_{\text{bb}}$. For a batch, this is $\mathbf{H}_{\text{bb}} \in \mathbb{R}^{B \times d_{p,\text{bb}}}$.

3. **Context and Conditioner Expansion:** $\mathbf{h}_{\text{bb}}^{(b)}$ is expanded to $\mathbf{H}_{\text{bb},\text{ex}}^{(b)} \in \mathbb{R}^{N_{\text{bb}} \times d_{p,\text{bb}}}$. $C_{\text{bb}}^{(b)}$ is used directly.
4. **MLP Input for Backbone Atoms:** For each backbone atom $j \in \mathcal{I}_{\text{bb}}$ in sample b , the input to the backbone MLP, MLP_{bb} , is:

$$M_{\text{in},\text{bb}}^{(b,j)} = \text{concat}(\mathbf{h}_{\text{bb}}^{(b)}, C_{\text{bb}}^{(b,j)}) \in \mathbb{R}^{d_{p,\text{bb}} + d_c}$$

5. **Backbone Coordinate Prediction:** A shared MLP_{bb} predicts backbone coordinates:

$$X_{\text{pred},\text{bb}}^{(b,j)} = \text{MLP}_{\text{bb}}(M_{\text{in},\text{bb}}^{(b,j)}) \in \mathbb{R}^3$$

This yields the predicted backbone structure $X_{\text{pred},\text{bb}} \in \mathbb{R}^{B \times N_{\text{bb}} \times 3}$.

C.2.2 Sidechain Decoder Stage

This stage predicts sidechain atom coordinates $X_{\text{pred},\text{sc}}$ using the full latent embeddings $Z^{(b)} \in \mathbb{R}^{N \times d_z}$, the conditioner $C^{(b)} \in \mathbb{R}^{N \times d_c}$, and the predicted backbone coordinates $X_{\text{pred},\text{bb}}^{(b)} \in \mathbb{R}^{B \times N_{\text{bb}} \times 3}$ from the Backbone Decoder Stage.

1. **Sidechain Embedding Selection:** Latent embeddings $Z_{\text{sc}}^{(b)} \in \mathbb{R}^{N_{\text{sc}} \times d_z}$ corresponding to sidechain atoms \mathcal{I}_{sc} are selected from the full latent embeddings $Z^{(b)}$.
2. **Sidechain Pooling:** The selected sidechain embeddings $Z_{\text{sc}}^{(b)}$ are pooled using a 2D adaptive average pooling layer \mathcal{P}_{sc} (e.g., `BlindPooling2D` with output size $H_{\text{sc}} \times W_{\text{sc}}$) to obtain a sidechain-specific context vector for each sample in the batch:

$$\mathbf{h}_{\text{sc}}^{(b)} = \mathcal{P}_{\text{sc}}(Z_{\text{sc}}^{(b)}) \in \mathbb{R}^{d_{p,\text{sc}}}$$

where $d_{p,\text{sc}} = H_{\text{sc}} \cdot W_{\text{sc}}$. For a batch, this results in $\mathbf{H}_{\text{sc}} \in \mathbb{R}^{B \times d_{p,\text{sc}}}$.

3. **Feature Construction for Sidechain MLP Input:** The input to the sidechain MLP, MLP_{sc} , is a global vector $M_{\text{in},\text{sc}}^{(b)}$ constructed per sample b . The construction varies based on the `arch_type`:

- Let $X_{\text{pred},\text{bb},\text{flat}}^{(b)} \in \mathbb{R}^{N_{\text{bb}} \cdot 3}$ be the flattened predicted backbone coordinates for sample b .

- Let $C_{\text{sc}}^{(b)} \in \mathbb{R}^{N_{\text{sc}} \times d_c}$ be the sidechain portion of the reference conditioner. If $d_c = d_z$, this is $Z_{\text{ref, sc}}^{(b)}$. This is flattened to $C_{\text{sc, flat}}^{(b)} \in \mathbb{R}^{N_{\text{sc}} \cdot d_c}$.

Arch-Type 0: The input consists of the flattened predicted backbone coordinates and the pooled sidechain context from the current frame’s embeddings.

$$M_{\text{in, sc}}^{(b)}[\text{Arch 0}] = \text{concat}(X_{\text{pred, bb, flat}}^{(b)}, \mathbf{h}_{\text{sc}}^{(b)})$$

The dimension of $M_{\text{in, sc}}^{(b)}[\text{Arch 0}]$ is $(N_{\text{bb}} \cdot 3) + d_{p, \text{sc}}$.

Arch-Type 1: This architecture adds a reduced representation of the sidechain portion of the reference conditioner.

- The flattened sidechain conditioner $C_{\text{sc, flat}}^{(b)}$ is passed through a linear reduction layer:

$$C_{\text{sc, reduced}}^{(b)} = \text{Linear}_{\text{sc, reduce}}(C_{\text{sc, flat}}^{(b)}) \in \mathbb{R}^{d'_{c, \text{sc}}}$$

(e.g., $d'_{c, \text{sc}} = 128$ in the implementation).

The MLP input is then:

$$M_{\text{in, sc}}^{(b)}[\text{Arch 1}] = \text{concat}(X_{\text{pred, bb, flat}}^{(b)}, \mathbf{h}_{\text{sc}}^{(b)}, C_{\text{sc, reduced}}^{(b)})$$

The dimension of $M_{\text{in, sc}}^{(b)}[\text{Arch 1}]$ is $(N_{\text{bb}} \cdot 3) + d_{p, \text{sc}} + d'_{c, \text{sc}}$.

Arch-Type 2: This architecture uses a reduced representation of both the predicted backbone coordinates and the sidechain portion of the reference conditioner.

- The flattened predicted backbone coordinates $X_{\text{pred, bb, flat}}^{(b)}$ are passed through a linear reduction layer:

$$X_{\text{pred, bb, reduced}}^{(b)} = \text{Linear}_{\text{bb, reduce}}(X_{\text{pred, bb, flat}}^{(b)}) \in \mathbb{R}^{d'_{\text{bb}}}$$

(e.g., $d'_{\text{bb}} = 128$ in the implementation).

- The sidechain conditioner is reduced as in Arch-Type 1 to $C_{\text{sc, reduced}}^{(b)} \in \mathbb{R}^{d'_{c, \text{sc}}}$.

The MLP input is then:

$$M_{\text{in, sc}}^{(b)}[\text{Arch 2}] = \text{concat}(X_{\text{pred, bb, reduced}}^{(b)}, \mathbf{h}_{\text{sc}}^{(b)}, C_{\text{sc, reduced}}^{(b)})$$

The dimension of $M_{\text{in, sc}}^{(b)}[\text{Arch 2}]$ is $d'_{\text{bb}} + d_{p, \text{sc}} + d'_{c, \text{sc}}$.

4. **Sidechain Coordinate Prediction:** The sidechain MLP, MLP_{sc} , processes the constructed input vector $M_{\text{in, sc}}^{(b)}$ (corresponding to the chosen `arch_type`) to predict all sidechain coordinates for sample b simultaneously:

$$X_{\text{pred, sc, flat}}^{(b)} = \text{MLP}_{\text{sc}}(M_{\text{in, sc}}^{(b)}) \in \mathbb{R}^{N_{\text{sc}} \cdot 3}$$

This flattened output is then reshaped to $X_{\text{pred, sc}}^{(b)} \in \mathbb{R}^{N_{\text{sc}} \times 3}$.

5. **Full Structure Assembly:** The final predicted structure $X_{\text{pred}}^{(b)} \in \mathbb{R}^{N \times 3}$ for sample b is assembled by combining the predicted backbone coordinates $X_{\text{pred, bb}}^{(b)}$ and the predicted sidechain coordinates $X_{\text{pred, sc}}^{(b)}$.

C.3 Residue-based Pooling Strategy

The Residue-based Pooling strategy generates a context vector specific to each residue and uses this local context for predicting the coordinates of atoms within that residue. Let $Z^{(b)} \in \mathbb{R}^{N \times d_z}$ be the latent atom embeddings for sample b . Let V_j be the set of atom indices belonging to residue R_j , and $f : V \rightarrow \{1, \dots, N_{\text{res}}\}$ be the mapping from a global atom index to its residue index.

1. **Per-Residue Pooling:** For each residue R_j in sample b :

- Select atom embeddings for residue R_j : $Z_{R_j}^{(b)} \in \mathbb{R}^{|V_j| \times d_z}$.

- Pool these embeddings using a 2D adaptive average pooling layer \mathcal{P}_{res} (e.g., `nn.AdaptiveAvgPool2d` with output $H \times W$):

$$\mathbf{h}_{R_j}^{(b)} = \mathcal{P}_{\text{res}}(Z_{R_j}^{(b)}) \in \mathbb{R}^{d_p}$$

where $d_p = H \cdot W$.

This results in a set of N_{res} pooled vectors for sample b , which can be represented as $\mathbf{H}_{\text{res}}^{(b)} \in \mathbb{R}^{N_{\text{res}} \times d_p}$. For a batch, this is $\mathbf{H}_{\text{res}} \in \mathbb{R}^{B \times N_{\text{res}} \times d_p}$.

2. **Atom-Specific Context Assembly:** For each atom i in sample b , its specific context vector is the pooled vector of its parent residue $R_{f(i)}$:

$$\mathbf{h}_{\text{atom_context}}^{(b,i)} = \mathbf{h}_{R_{f(i)}}^{(b)} \in \mathbb{R}^{d_p}$$

This can be gathered for all atoms to form $\mathbf{H}_{\text{atom_context}}^{(b)} \in \mathbb{R}^{N \times d_p}$.

3. **Conditioner Expansion:** The conditioner $C \in \mathbb{R}^{N \times d_c}$ is expanded for the batch to $C_{\text{ex}} \in \mathbb{R}^{B \times N \times d_c}$.
4. **MLP Input Formulation:** For each atom i in sample b , the input to the final MLP, MLP_{res} , is formed by concatenating its residue’s pooled context and its specific conditioner vector:

$$M_{\text{in, res}}^{(b,i)} = \text{concat}(\mathbf{h}_{\text{atom_context}}^{(b,i)}, C^{(b,i)}) \in \mathbb{R}^{d_p + d_c}$$

5. **Coordinate Prediction:** A shared MLP_{res} processes $M_{\text{in, res}}^{(b,i)}$ for each atom to predict its 3D coordinates:

$$X_{\text{pred}}^{(b,i)} = \text{MLP}_{\text{res}}(M_{\text{in, res}}^{(b,i)}) \in \mathbb{R}^3$$

This results in the full predicted structure $X_{\text{pred}} \in \mathbb{R}^{B \times N \times 3}$.

This strategy allows the model to learn representations that are localized at the residue level, potentially capturing residue-specific conformational preferences more directly.

D Latent Diffusion Model Details

This section details the Denoising Diffusion Probabilistic Model (DDPM) [47] utilized in our framework. The DDPM operates on the pooled latent embeddings $\mathbf{h}_0 \in \mathbb{R}^{d_p}$ (where d_p is the dimension of the pooled latent space, dependent on the pooling strategy) obtained from the encoder and pooling stages. Specific architectures and hyperparameters for the denoising network ϵ_θ are discussed in the Extended Technical Appendix (Section I).

D.1 DDPM Formulation

The DDPM consists of a predefined forward noising process and a learned reverse denoising process.

Forward Process (Noising): The forward process gradually adds Gaussian noise to an initial latent embedding \mathbf{h}_0 over T discrete timesteps. At each timestep t , the transition is defined by:

$$q(\mathbf{h}_t | \mathbf{h}_{t-1}) = \mathcal{N}(\mathbf{h}_t; \sqrt{1 - \beta_t} \mathbf{h}_{t-1}, \beta_t \mathbf{I})$$

where $\{\beta_t\}_{t=1}^T$ is a predefined variance schedule (e.g., linear, cosine) that controls the noise level at each step. A useful property of this process is that we can sample \mathbf{h}_t at any arbitrary timestep t directly from \mathbf{h}_0 :

$$q(\mathbf{h}_t | \mathbf{h}_0) = \mathcal{N}(\mathbf{h}_t; \sqrt{\bar{\alpha}_t} \mathbf{h}_0, (1 - \bar{\alpha}_t) \mathbf{I})$$

where $\alpha_t = 1 - \beta_t$ and $\bar{\alpha}_t = \prod_{s=1}^t \alpha_s$. As $t \rightarrow T$, if the schedule is chosen appropriately, \mathbf{h}_T approaches an isotropic Gaussian distribution $\mathcal{N}(0, \mathbf{I})$.

Reverse Process (Denoising): The reverse process aims to learn the transition $q(\mathbf{h}_{t-1} | \mathbf{h}_t)$, which is intractable directly. Instead, a neural network, $\epsilon_\theta(\mathbf{h}_t, t)$, is trained to predict the noise component ϵ that was added to \mathbf{h}_0 to produce $\mathbf{h}_t = \sqrt{\bar{\alpha}_t} \mathbf{h}_0 + \sqrt{1 - \bar{\alpha}_t} \epsilon$, where $\epsilon \sim \mathcal{N}(0, \mathbf{I})$. The network is optimized by minimizing the simplified DDPM loss function (as shown in Eq. 2 in the main text):

$$\mathcal{L}_{\text{diffusion}}(\theta) = \mathbb{E}_{t, \mathbf{h}_0, \epsilon} [\|\epsilon - \epsilon_\theta(\sqrt{\bar{\alpha}_t} \mathbf{h}_0 + \sqrt{1 - \bar{\alpha}_t} \epsilon, t)\|^2]$$

where t is sampled uniformly from $\{1, \dots, T\}$.

D.2 Sampling New Latent Embeddings

Once the denoising network ϵ_θ is trained, new latent embeddings $\mathbf{h}_0^{\text{gen}}$ can be generated by starting with a sample from the prior distribution, $\mathbf{h}_T \sim \mathcal{N}(0, \mathbf{I})$, and iteratively applying the reverse denoising step:

$$\mathbf{h}_{t-1} = \frac{1}{\sqrt{\alpha_t}} \left(\mathbf{h}_t - \frac{\beta_t}{\sqrt{1-\alpha_t}} \epsilon_\theta(\mathbf{h}_t, t) \right) + \sigma_t \mathbf{z}$$

where $\mathbf{z} \sim \mathcal{N}(0, \mathbf{I})$ for $t > 1$, and $\mathbf{z} = 0$ for $t = 1$. The variance σ_t^2 is typically set to β_t or $\tilde{\beta}_t = \frac{1-\alpha_{t-1}}{1-\alpha_t} \beta_t$. The full sampling procedure is outlined in Algorithm 2.

Algorithm 2 Reverse Diffusion Sampling for Latent Embeddings

- 1: **Input:** Trained denoising model ϵ_θ , number of generation samples B_{gen} , dimension of pooled latent d_p , diffusion timesteps T , schedule parameters (e.g., β_1, \dots, β_T).
 - 2: Calculate $\alpha_t = 1 - \beta_t$ and $\bar{\alpha}_t = \prod_{s=1}^t \alpha_s$ for all t .
 - 3: Set $\sigma_t^2 = \beta_t$ (or alternative like $\tilde{\beta}_t$).
 - 4: Sample initial noise $\mathbf{h}_T \sim \mathcal{N}(0, \mathbf{I})$ of shape (B_{gen}, d_p) .
 - 5: **for** $t = T, \dots, 1$ **do**
 - 6: Sample $\mathbf{z} \sim \mathcal{N}(0, \mathbf{I})$ of shape (B_{gen}, d_p) if $t > 1$, else $\mathbf{z} = \mathbf{0}$.
 - 7: Predict noise: $\epsilon_{\text{pred}} \leftarrow \epsilon_\theta(\mathbf{h}_t, t)$
 - 8: Calculate conditional mean: $\mu_\theta(\mathbf{h}_t, t) = \frac{1}{\sqrt{\alpha_t}} \left(\mathbf{h}_t - \frac{\beta_t}{\sqrt{1-\alpha_t}} \epsilon_{\text{pred}} \right)$
 - 9: Update latent sample: $\mathbf{h}_{t-1} \leftarrow \mu_\theta(\mathbf{h}_t, t) + \sigma_t \mathbf{z}$
 - 10: **end for**
 - 11: **Output:** Generated latent embeddings $\mathbf{h}_0^{\text{gen}} = \mathbf{h}_0$
-

E Loss Function Formulations

This section provides the detailed mathematical formulations for the loss functions used in the LD-FPG framework. The notation used is consistent with Appendix A.1.

E.1 Encoder Pre-training Loss

The pre-training phase for the ChebNet encoder (Encoder_θ) can be performed using a direct coordinate reconstruction head (MLP_{HNO}). The loss function \mathcal{L}_{HNO} is the Mean Squared Error (MSE) between the predicted coordinates and the ground truth coordinates:

$$\mathcal{L}_{\text{HNO}} = \mathbb{E}_{(X_{\text{true}}, Z) \sim \mathcal{D}} [\|\text{MLP}_{\text{HNO}}(Z) - X_{\text{true}}\|_F^2] \quad (3)$$

where $Z = \text{Encoder}_\theta(X_{\text{true}}, E)$, \mathcal{D} is the training dataset, and $\|\cdot\|_F^2$ denotes the squared Frobenius norm (sum of squared element-wise differences). For a single sample with N atoms, this is $\frac{1}{N} \sum_{i=1}^N \|\text{MLP}_{\text{HNO}}(Z_i) - (X_{\text{true}})_i\|^2$.

E.2 Decoder Loss Functions

E.2.1 Coordinate Mean Squared Error ($\mathcal{L}_{\text{coord}}$)

This is the fundamental loss for all decoder architectures, measuring the MSE between predicted coordinates X_{pred} and ground truth coordinates X_{true} :

$$\mathcal{L}_{\text{coord}} = \mathbb{E}_{(X_{\text{true}}, X_{\text{pred}}) \sim \mathcal{D}_{\text{dec}}} [\|X_{\text{pred}} - X_{\text{true}}\|_F^2] \quad (4)$$

For a single sample, this is $\frac{1}{N} \sum_{i=1}^N \|(X_{\text{pred}})_i - (X_{\text{true}})_i\|^2$.

E.2.2 Dihedral Angle Mean Squared Error ($\mathcal{L}_{\text{mse.dih}}$)

This loss penalizes the squared difference between predicted dihedral angles (α_{pred}) and true dihedral angles (α_{true}). It is used *only* for fine-tuning the Blind Pooling decoder.

$$\mathcal{L}_{\text{mse.dih}} = \sum_{\alpha \in \mathcal{A}} \mathbb{E}_{(b,j) | M_\alpha(j)} \left[(\alpha_{\text{pred}}^{(b,j)} - \alpha_{\text{true}}^{(b,j)})^2 \right] \quad (5)$$

where \mathcal{A} is the set of all considered dihedral angle types (e.g., $\phi, \psi, \chi_1, \dots, \chi_5$), $M_\alpha(j)$ is a mask indicating if angle type α is valid for residue j in sample b . The expectation is over valid angles in the batch.

E.2.3 Dihedral Angle Distribution Divergence ($\mathcal{L}_{\text{div.dih}}$)

This loss encourages the empirical distribution of predicted dihedral angles ($P(\alpha_{\text{pred}})$) to match that of the true angles ($P(\alpha_{\text{true}})$). It is used *only* for fine-tuning the blind pooling decoder.

$$\mathcal{L}_{\text{div.dih}} = \sum_{\alpha \in \mathcal{A}} D_{\text{KL}}(P(\alpha_{\text{pred}}) \| P(\alpha_{\text{true}})) \quad (6)$$

where D_{KL} is the Kullback-Leibler divergence (or optionally Jensen-Shannon divergence, JSD, or Wasserstein Distance, WD, as specified in hyperparameters). The distributions $P(\cdot)$ are typically estimated from histograms of angles within a batch or across a larger set of samples.

E.2.4 Combined Decoder Loss (\mathcal{L}_{Dec})

The definition of \mathcal{L}_{Dec} depends on the pooling strategy:

Blind Pooling Decoder:

- **Initial Training:** The decoder is trained solely on coordinate MSE:

$$\mathcal{L}_{\text{Dec}}^{\text{Blind, initial}} = \mathcal{L}_{\text{coord}}$$

- **Fine-tuning (Optional):** The loss becomes a weighted sum, where dihedral terms are applied stochastically (e.g., to 10% of mini-batches, controlled by f_{dih}):

$$\mathcal{L}_{\text{Dec}}^{\text{Blind, fine-tune}} = w_{\text{base}} \cdot \mathcal{L}_{\text{coord}} + S \cdot (\lambda_{\text{mse}} \cdot \mathcal{L}_{\text{mse.dih}} + \lambda_{\text{div}} \cdot \mathcal{L}_{\text{div.dih}})$$

where $S = 1$ with probability f_{dih} and $S = 0$ otherwise. w_{base} , λ_{mse} , and λ_{div} are scalar weights.

Residue-based Pooling Decoder: This decoder is trained using only the coordinate MSE loss:

$$\mathcal{L}_{\text{Dec}}^{\text{Residue}} = \mathcal{L}_{\text{coord}}$$

E.2.5 Sequential Pooling Decoder Losses

The sequential pooling strategy uses two separate MSE-based losses:

- **Backbone Decoder Loss (\mathcal{L}_{BB}):** This is the coordinate MSE loss applied specifically to the predicted backbone atom coordinates $X_{\text{pred,bb}}$ against the true backbone coordinates $X_{\text{true,bb}}$:

$$\mathcal{L}_{\text{BB}} = \mathbb{E}_{(X_{\text{true,bb}}, X_{\text{pred,bb}}) \sim \mathcal{D}_{\text{dec}}} [\|X_{\text{pred,bb}} - X_{\text{true,bb}}\|_F^2]$$

This corresponds to applying $\mathcal{L}_{\text{coord}}$ only to atoms $i \in \mathcal{I}_{\text{bb}}$.

- **Sidechain Decoder (Full Structure) Loss (\mathcal{L}_{SC}):** After the Sidechain Decoder predicts sidechain coordinates and assembles the full structure X_{pred} , this loss is the coordinate MSE for the entire protein structure:

$$\mathcal{L}_{\text{SC}} = \mathbb{E}_{(X_{\text{true}}, X_{\text{pred}}) \sim \mathcal{D}_{\text{dec}}} [\|X_{\text{pred}} - X_{\text{true}}\|_F^2]$$

This is equivalent to $\mathcal{L}_{\text{coord}}$ applied to the output of the complete two-stage sequential decoder.

Neither \mathcal{L}_{BB} nor \mathcal{L}_{SC} include dihedral angle terms in their standard formulation for the sequential pooling decoder.

F Experimental Setup Details

This appendix provides further details on the dataset, evaluation metrics, and implementation aspects of the experimental setup.

F.1 Dataset and MD Simulation Protocol

The conformational dataset for the human Dopamine D2 receptor (D2R) was generated from all-atom Molecular Dynamics (MD) simulations. **System Preparation:** Simulations were initiated from the cryo-EM structure of the D2R in complex with the inverse agonist risperidone (PDB ID: 6CM4 [66]). The risperidone ligand was removed, and the third intracellular loop (ICL3), which is typically flexible or unresolved, was remodeled using RosettaRemodel [67] to represent an apo-like state. The final remodeled D2R structure consisted of 273 residues, comprising 2191 heavy atoms after selection for the simulation system; hydrogen atoms were not explicitly included as input features to our generative model, which focuses on heavy-atom representations. The D2R protein was then embedded in a 1-palmitoyl-2-oleoyl-sn-glycero-3-phosphocholine (POPC) lipid bilayer using the CHARMM-GUI *Membrane Builder* [68]. The system was solvated with TIP3P water [69] and neutralized with 0.15 M NaCl ions. **Simulation Parameters:** The CHARMM36m force field [70] was employed for all protein, lipid, and ion parameters. Simulations were performed using GRO-MACS 2024.2 [71]. The system underwent energy minimization followed by a multi-step equilibration protocol involving NVT and NPT ensembles with position restraints on the protein heavy atoms, which were gradually released. Production simulations were run under the NPT ensemble at 303.15 K (using the v-rescale thermostat [72]) and 1.0 bar (using the C-rescale barostat [73] with semi-isotropic coupling). A 2 fs timestep was used, with LINCS algorithm [74] constraining bonds involving hydrogen atoms. Electrostatic interactions were calculated using the Particle Mesh Ewald (PME) method [75]). **Trajectory Processing:** Ten independent production replicas, each 2 μ s in length, were generated. One replica exhibiting representative dynamics was selected for this study. The initial ≈ 776 ns of this replica were discarded as extended equilibration, yielding a final analysis trajectory of ≈ 1.224 μ s. From this, 12,241 frames were sampled at a regular interval of 100 ps. All protein heavy-atom coordinates in these frames were then rigidly aligned to the heavy atoms of the first frame using the Kabsch algorithm [56] to remove global translation and rotation. **Data Splitting and Preprocessing:** The aligned coordinate dataset was split into a training set (90%, 11,017 frames) and a test set (10%, 1,224 frames) chronologically. Static topological information, including lists of backbone and sidechain atom indices based on a consistent re-indexing scheme, and the definitions of atom quadruplets for standard dihedral angles ($\phi, \psi, \chi_1 - \chi_5$), was extracted once from the reference PDB structure. This information was stored in JSON format as detailed in Appendix B.

F.2 Evaluation Metrics

Model performance was assessed using the following metrics:

F.2.1 Coordinate Accuracy

- **Mean Squared Error ($\text{MSE}_{\text{bb}}, \text{MSE}_{\text{sc}}$):** Calculated as the average squared Euclidean distance between predicted and ground truth coordinates for corresponding atoms. MSE_{bb} considers $\text{C}\alpha$ atoms (or all backbone heavy atoms N, CA, C, O, as specified in implementation) and MSE_{sc} considers all sidechain heavy atoms. The MSE for a set of N_k atoms (either backbone or sidechain) is: $\text{MSE} = \frac{1}{N_k} \sum_{i=1}^{N_k} \|\mathbf{x}_{\text{pred},i} - \mathbf{x}_{\text{true},i}\|^2$.
- **Local Distance Difference Test (IDDT) [76]:** IDDT evaluates the preservation of local interatomic distances. For each atom, it considers all other atoms within a defined cutoff radius (e.g., 15 Å) in the reference (true) structure. It then calculates the fraction of these interatomic distances that are preserved in the predicted structure within certain tolerance thresholds (e.g., 0.5, 1, 2, and 4 Å). The final IDDT score is an average over these fractions and all residues/atoms. We report IDDT_{All} (all heavy atoms on backbone and sidechain) and IDDT_{BB} (backbone heavy atoms). Scores range from 0 to 1, with 1 indicating perfect preservation.
- **Template Modeling score (TM-score) [77]:** TM-score measures the global structural similarity between a predicted model and a reference structure. It is designed to be more sensitive to correct global topology and less sensitive to local errors than RMSD, and its value is normalized to be between 0 and 1, where 1 indicates a perfect match. A TM-score ≥ 0.5 generally indicates that the two proteins share a similar fold.

F.2.2 Distributional Accuracy

- **Summed Kullback–Leibler Divergence ($\sum \text{KL}$) and Jensen–Shannon Divergence ($\sum \text{JSD}$):** These metrics quantify the similarity between the 1D distributions of predicted and ground truth dihedral angles (ϕ , ψ , and χ_1 through χ_5). For each angle type, empirical probability distributions are estimated from histograms (e.g., using 36 bins over the range $[-\pi, \pi]$). The KL or JS divergence is calculated for each angle type, and the reported $\sum \text{KL}$ or $\sum \text{JSD}$ is the sum of these divergences over all seven angle types. Lower values indicate higher similarity between the distributions.

F.2.3 Physical Plausibility

- **Average Steric Clash Counts:** A steric clash is defined as a pair of non-bonded heavy atoms being closer than a specified distance cutoff. For our analysis, we used a cutoff of 2.1 Å. The clash score is the average number of such clashing pairs per generated structure. This metric was computed using BioPython [78] and SciPy’s [79] cKDTree for efficient neighbor searching.

F.2.4 Conformational Landscape Sampling

- **A100 Activation Index Value:** The A100 value is a collective variable developed by Ibrahim et al. [57] to quantify the activation state of Class A G-protein-coupled receptors (GPCRs). It is a linear combination of five specific interhelical C α -C α distances that are known to change upon GPCR activation. The formula is given by:

$$\begin{aligned} A^{100} = & -14.43 \times r(V^{1.53}-L^{7.55}) - 7.62 \times r(D^{2.50}-T^{3.37}) \\ & + 9.11 \times r(N^{3.42}-I^{4.42}) - 6.32 \times r(W^{5.66}-A^{6.34}) \\ & - 5.22 \times r(L^{6.58}-Y^{7.35}) + 278.88 \end{aligned}$$

where $r(X^{\text{BW}_1}-Y^{\text{BW}_2})$ denotes the distance in Angstroms between the C α atoms of residue X at Ballesteros-Weinstein (BW) position BW₁ and residue Y at BW position BW₂. Higher A100 values typically correspond to more active-like states. We use this metric to compare the conformational landscape explored by generated ensembles against the reference MD simulation.

- **Principal Component Analysis (PCA) of Latent Embeddings:** PCA is applied to the set of pooled latent embeddings (\mathbf{h}_0) generated by the diffusion model and those derived from the MD dataset. Projecting these high-dimensional embeddings onto the first few principal components allows for a 2D visualization, which helps assess whether the generative model captures the diversity and main modes of variation present in the training data’s latent space.

F.2.5 Training Loss Reporting

- **Auxiliary Dihedral MSE Term ($\sum \mathcal{L}_{\text{dih}}$ MSE):** When dihedral losses are active during the fine-tuning of the blind pooling decoder (see Appendix E for $\mathcal{L}_{\text{mse.dih}}$), we report the sum of the training MSE losses for all considered dihedral angles. This provides insight into how well the model fits these auxiliary geometric targets.

F.3 Training resources

The input Molecular Dynamics (MD) data was generated using GROMACS 2024.2 [71] on NVIDIA L40S GPUs. With a simulation rate of approximately 250 ns/day, the 2 micro seconds trajectory used in this study required about 8 days of computation. Following data generation, all machine learning models were implemented in PyTorch [58] and trained using the Adam optimizer [59] on NVIDIA L40S and H100 GPUs. The ChebNet autoencoder training required approximately 5,000 epochs at roughly 2 seconds per epoch. Decoder training varied by pooling strategy: blind pooling decoders trained for 3,000-6,000 epochs at approximately 3 seconds per epoch, while residue pooling decoders took about 24 seconds per epoch for a similar number of epochs. Diffusion model training was the most computationally intensive: sequential and blind pooling models trained for around 10,000 epochs, and residue pooling models for up to 150,000 epochs, with each epoch averaging approximately 1 second on L40S GPUs. The machine learning aspects presented in this paper required approximately 15,000 GPU hours, with total experimentation including preliminary setups

amounting to roughly 30,000 GPU hours. This substantial GPU usage translates to significant energy consumption and associated carbon emissions; while precise quantification depends on factors like data center Power Usage Effectiveness (PUE) and local energy grid carbon intensity (and was not performed for this study), we acknowledge this environmental cost. Further details on computational resources, including specific MD simulation parameters and machine learning training runtimes for hyperparameter sweeps, are provided in the Extended Technical Appendix (Appendix I). The overall three-phase training and generation workflow (encoder pre-training, decoder training, and diffusion model training) is detailed in Appendix A (Algorithm 1).

G Encoder Performance Summary

The ChebNet encoder’s reconstruction head performance provides an upper bound on achievable fidelity. Table 3 summarizes key metrics for different latent dimensions (d_z). The encoder accurately captures structural features and dihedral angle distributions with minimal deviation from the ground truth MD data.

Table 3: Encoder Reconstruction Head Performance.

Encoder Config	IDDT _{All} ↑	IDDT _{BB} ↑	TM _{All} ↑	\sum JSD _{bb} ↓	\sum JSD _{sc} ↓	MSE _{bb} ↓	MSE _{sc} ↓	$\sum \mathcal{L}_{\text{dih}}$ MSE ↓
Encoder ($d_z = 4$)	0.692	0.777	0.959	0.00005	0.0002	0.0040	0.00715	0.00066
Encoder ($d_z = 8$)	0.697	0.780	0.959	0.00069	0.0009	0.0021	0.00375	0.00188
Encoder ($d_z = 16$)	0.696	0.782	0.959	0.00009	0.00016	0.0008	0.00160	0.00058
GT (MD) Ref	0.698	0.779	0.959	-	-	-	-	-

H Residue Pooling Inference Details

For the residue pooling model visualizations (Fig. 2c and Fig. 4c in the main text), samples were aggregated from 10 distinct model checkpoints saved at different stages of the diffusion model’s training. This multi-epoch sampling strategy, inspired by moving average techniques [80], was employed to provide a more stable and representative visualization of the learned conformational space, averaging out potential epoch-specific biases.

I Extended Technical Appendix

This Extended Technical Appendix provides a deeper dive into the experimental methodology, specific hyperparameter choices that led to the main paper’s results, additional sensitivity analyses, and information regarding the availability of code and datasets used in this work. The sections are organized as follows:

- **Code and Data Availability** (Section I.1): Links to the LD-FPG implementation and the D2R-MD dataset.
- **Estimated CO₂-equivalent emissions** (Section I.2): Discussion on the computational resources and environmental impact.
- **ChebNet Encoder Details and Ablation** (Sections I.3 and I.4): Parameters for the encoder used in main results and a sensitivity analysis on its key hyperparameters (k , K , d_z).
- **Decoder Architectures and Configurations** (Section I.5): Detailed configurations for Blind, Sequential, and Residue pooling strategies corresponding to main paper results (Tables 1 and 2), including final chosen pooling dimensions and dihedral loss settings for Blind Pooling fine-tuning. This is supplemented by illustrative hyperparameter scan examples for Blind Pooling decoders (Section I.7).
- **Latent Diffusion Model Details** (Sections I.6 and I.8): Overview of diffusion model configurations and example hyperparameter scans for the Blind Pooling strategy.
- **Conditioning Mechanism Tuning** (Section I.9): Ablation study results for the decoder conditioning mechanism.
- **Discussion on Metric Variability** (Section I.10): Contextualization of standard deviations for reported performance metrics.

While comprehensive hyperparameter sweeps were conducted for all components and strategies, due to space constraints, we primarily showcase detailed scan results for the Blind Pooling strategy to illustrate the optimization process. Similar systematic approaches were employed for other strategies. For exhaustive details beyond what is presented, readers are encouraged to consult the provided codebase or contact the authors.

I.1 Code and Data Availability

To facilitate reproducibility and further research, the LD-FPG implementation (including scripts for data preprocessing, model training, and evaluation) is made available at:

- **Code (LD-FPG)**: <https://github.com/adityasengar/LD-FPG>

The D2R-MD dataset, comprising the 2 μ s MD trajectory (12,241 frames) of the human dopamine D2 receptor used in this study, is available at:

- **Dataset (D2R-MD)**: <https://zenodo.org/records/15479781>

The dataset includes aligned heavy-atom coordinates and pre-calculated dihedral angles, along with the necessary topology files as described in Appendix B.

I.2 Estimated CO₂-equivalent emissions

To provide a transparent measure of the environmental cost of our computational pipeline, we estimate the operational (Scope-2) footprint of the $\sim 30,000$ GPU-hours consumed in this work. This total compute time was a mix of NVIDIA H100 and L40S GPUs. For our typical training workloads, H100 GPUs offered a significant speed-up, completing tasks in roughly half the time compared to L40S GPUs. For instance, a ChebNet autoencoder training of 5,000 epochs took approximately 2 seconds per epoch on an H100 GPU (totaling ~ 2.8 H100-hours for one such run).

Following [81], the *per-GPU-hour* emissions are:

$$\text{kg CO}_2\text{e} = \left(\frac{P_{\text{board}}}{1000} \right) \times u \times \text{PUE} \times \text{CI}, \quad (7)$$

where P_{board} is the vendor-specified board power, u is the average utilisation of that cap, PUE is the data-centre power usage effectiveness, and CI is the grid carbon intensity.

Assumptions. Board powers were taken from the NVIDIA L40S datasheet ($P = 350$ W) [82] and the H100 SXM-5 specification ($P = 700$ W) [83]. We adopt a conservative mean utilisation $u = 0.8$, and a modern colocation PUE of 1.30, which is below the current global fleet average of 1.56 but well within the range observed for new facilities [84]. For the electricity mix we give two reference cases: (i) the 2022 global mean ($\text{CI} = 0.436 \text{ kg CO}_2\text{e kWh}^{-1}$) derived from Ember’s Global Electricity Review [85], and (ii) the Swiss consumption-based factor of $0.112 \text{ kg CO}_2\text{e kWh}^{-1}$ for the same year, which captures the low-carbon hydro–nuclear mix and net imports [86].

Results. Table 4 summarises six scenarios. The ”all-L40S” and ”all-H100” scenarios are hypotheticals where the entire 30,000 GPU-hours were run on a single GPU type. More realistically, a mix of GPUs was used. For an illustrative scenario, we consider a split where 70% of the total operational hours (21,000 hours) were logged on L40S GPUs and 30% (9,000 hours) on H100 GPUs. The energy consumption for this specific split is calculated as the sum of energy consumed by each GPU type for their respective hours. Even the worst-case (all-H100 on the global-average grid) remains on the order of a single round-trip transatlantic flight for two passengers, while execution on a Swiss-like grid cuts emissions by $\sim 4\times$.

Table 4: Estimated operational CO_2e emissions for the $\sim 30,000$ GPU-hours used in this study. Energy is computed as $(P_{\text{board}}/1000) \times \text{Hours} \times u \times \text{PUE}$, with $u = 0.8$ and $\text{PUE} = 1.30$. For the 70/30 split, L40S = 21,000 hours; H100 = 9,000 hours.

Scenario	Energy (kWh)	Grid CI (kg/kWh)	PUE	tCO ₂ e
All L40S (30k hrs)	10,920	0.436	1.30	4.8
All H100 (30k hrs)	21,840	0.436	1.30	9.5
70% L40S / 30% H100	14,196	0.436	1.30	6.2
L40S (Swiss mix)	10,920	0.112	1.30	1.2
H100 (Swiss mix)	21,840	0.112	1.30	2.4
70% L40S / 30% H100 (Swiss)	14,196	0.112	1.30	1.6

Context and mitigation. These figures exclude embodied (Scope-3) emissions of the hardware itself, which may add $\sim 2\text{--}3 \text{ tCO}_2\text{e}$ over its lifetime. Practitioners can further reduce impact by (a) scheduling training in regions with low-carbon grids, (b) capping GPU power (the H100 supports dynamic 350–700 W limits), (c) early stopping during training and (d) prioritising model efficiency improvements that reduce GPU runtime.

I.3 Graph Construction and ChebNet Encoder Parameters for Main Results

For each MD frame, the graph edge index $E^{(t)}$ was constructed using a k -Nearest Neighbors search with $k = 4$ on the aligned coordinates. This value of k was chosen as it was found to maintain graph connectivity effectively while managing computational cost for graph construction at each step. The ChebNet encoder (Section 3.2) utilizes Chebyshev polynomials up to order $K = 4$. The network comprises $L_{\text{ChebNet}} = 4$ ChebConv layers. The first two layers use LeakyReLU activations, the third employs ReLU, and BatchNorm1d is applied after each ChebConv layer. The final layer’s output, the atom-wise latent embeddings $Z^{(t)}$, is L_2 normalized. The encoder latent dimension d_z was varied for different pooling strategies, with $d_z \in \{4, 8, 16\}$ being explored. The specific d_z values used for the main results with each pooling strategy are detailed in Section I.5. Key parameters for the ChebNet encoder architecture and its pre-training regimen are summarized in Table 5.

I.4 ChebNet Encoder Ablation: k-NN, Chebyshev Order (K), and Latent Dimension (d_z)

This subsection details an ablation study conducted on the ChebNet autoencoder to explore the impact of varying key graph construction and architectural parameters: the number of nearest neighbors (k) for graph construction, the Chebyshev polynomial order (K), and the latent dimension (d_z). For

Table 5: ChebNet Encoder Model parameters and training Hyperparameters used for generating main paper results.

Parameter	Value(s)
Input Features	3 (Coordinates)
Number of Atoms (N, D2R)	2191
kNN Graph k (k)	4
ChebConv Order (K)	4
Number of Layers (L_{ChebNet})	4
Hidden Dimension (d_z)	Tuned per pooling (see Sec. I.5: 4, 8, or 16)
Activation (L1, L2)	
Activation (L3)	
Normalization	BatchNorm1d
Final Embedding Norm	L2
Optimizer	Adam
Learning Rate	1e-4
Batch Size	16
Epochs (Pre-training)	4000
Dihedral Loss during Pre-training	Disabled

each parameter combination presented in Table 6, the ChebNet autoencoder was trained for approximately 24 hours, and we report the final test loss (coordinate MSE) achieved and the average time per epoch.

It is important to note that if the performance figures here, particularly the final test losses, differ from those presented in Appendix G (Table 3), it is primarily because the encoder models in Appendix G were trained for a fixed 5000 epochs using specific parameters ($k = 4, K = 4$) which we determined yielded a sufficiently low MSE for subsequent stages of the LD-FPG pipeline. The experiments here, with a fixed 24-hour training budget, provide a different perspective on parameter sensitivity under time-constrained training.

The results in Table 6 demonstrate that the ChebNet autoencoder architecture is capable of achieving low reconstruction loss across a range of parameter settings. Generally, increasing the latent dimension d_z tends to decrease the final test loss, albeit with a slight increase in epoch time. The influence of k and K is more nuanced, showing that different combinations can yield strong performance. For instance, with $K = 4$, increasing k from 4 to 8 and then to 16, particularly for $d_z = 16$, resulted in the lowest test loss (0.000110) in this set of experiments ($K = 4, k = 8, d_z = 16$). Higher orders of K (e.g., $K = 8, 16$) also show competitive losses but come with a more significant increase in epoch computation time.

Based on these findings, the ChebNet autoencoder effectively reduces reconstruction loss under various conditions. Users and researchers are encouraged to explore these parameters to optimize performance for their specific protein systems and computational budgets. The subsequent pooling strategies (Blind, Sequential, and Residue pooling) and the main results presented in this paper were developed based on our preliminary analyses which utilized $K = 4$ and $k = 4$. This choice offered a good balance between model performance and the computational cost associated with graph construction and training, especially for the extensive MD datasets used.

Table 6: ChebNet Encoder Ablation Study Results. Each configuration was trained for approximately 24 hours.

Chebyshev Order (K)	k-NN Value (k)	Hidden Dim (d_z)	Avg Epoch Time (s)	Final Test Loss
4	4	4	4.63	0.001756
4	4	8	4.66	0.000184
4	4	16	4.74	0.000263
4	8	4	4.74	0.000371
4	8	8	4.70	0.000373
4	8	16	4.97	0.000110
4	16	4	5.45	0.001016
4	16	8	5.20	0.000387
4	16	16	5.91	0.000226
8	4	4	6.99	0.000448
8	4	8	6.91	0.000698
8	4	16	7.08	0.000649
8	8	4	7.16	0.000624
8	8	8	7.13	0.000562
8	8	16	7.34	0.000545
8	16	4	7.52	0.000256
8	16	8	7.68	0.000256
8	16	16	10.73	0.001494
16	4	4	11.52	0.000262
16	4	8	11.38	0.000484
16	4	16	11.81	0.001428
16	8	4	11.86	0.003231
16	8	8	11.55	0.001885
16	8	16	12.27	0.000741
16	16	4	12.82	0.003709
16	16	8	14.89	0.001196
16	16	16	17.49	0.003388

I.5 Decoder Architectures: General Configuration and Key Parameters for Main Results

All decoder architectures map atom-wise latent embeddings Z and a conditioner $C = Z_{\text{ref}}$ (the latent embedding of the reference structure X_{ref}) to Cartesian coordinates X_{pred} . General training parameters for decoders included the Adam optimizer, a batch size of 16, and initial training for 5000 epochs with a learning rate of 3×10^{-4} , unless specified otherwise for fine-tuning or specific pooling strategies.

Blind Pooling Strategy Details Atom-wise embeddings $Z^{(t)}$ are globally pooled using 2D adaptive average pooling to a target dimension $d_p = H \times W$. This global context, expanded per-atom, is concatenated with C and fed to an MLP (MLP_{blind}) with ReLU activations and BatchNorm1d. The configuration that yielded the main paper results for Blind Pooling ($d_z = 16$, Tables 1 & 2) is detailed in Table 7. This table also includes the parameters for the dihedral fine-tuning stage. Detailed hyperparameter scans for the Blind Pooling decoder MLP varying H , W , and N_{layers} are presented in Section I.7.

Sequential Pooling Strategy Details ($d_z = 8$) This strategy involves a BackboneDecoder followed by a SidechainDecoder.

- **Backbone Decoder Stage Configuration (for Tables 1 & 2):**
 - Pooling: Backbone-specific atom embeddings ($d_z = 8$) were pooled to $d_{p,bb} = H_{bb} \times W_{bb} = 45 \times 3 = 135$.
- **Sidechain Decoder Stage Configuration (for Tables 1 & 2):**

Table 7: Blind Pooling Decoder Hyperparameters for Main Paper Results ($d_z = 16$).

Parameter	Value
Encoder Latent Dim (d_z)	16
Conditioner (C)	Z_{ref}
Pooling Type	Blind
Pooling Height (H)	50
Pooling Width (W)	2
Pooled Dimension (d_p)	100
MLP Hidden Dimension	128
MLP Total Layers (N_{layers})	12
MLP Activation	ReLU
MLP Normalization	BatchNorm1d
Optimizer	Adam
Learning Rate (Initial)	3e-4
Batch Size	16
Epochs (Initial Training)	5000
<i>Fine-tuning with Dihedral Loss (for Table 1)</i>	
Base Coord Weight (w_{base})	1.0
Dihedral Loss Enabled	Yes
Stochastic Fraction (f_{dih})	0.1
Dihedral Divergence Type	KL
Dihedral MSE Weight (λ_{mse})	0.00
Dihedral Div Weight (λ_{div})	2.00
Epochs (Fine-tuning)	2000
Torsion Info File	condensed_residues.json

- Architecture: `arch_type=1` (see Appendix C.2.2).
- Pooling: Sidechain-specific atom embeddings ($d_z = 8$) were pooled to $d_{p,sc} = H_{sc} \times W_{sc} = 54 \times 2 = 108$.

Residue Pooling Strategy Details ($d_z = 4$) Per-residue atom embeddings $Z_{R_j}^{(t)}$ are pooled to local contexts $z_{\text{res},j}$.

• **Decoder Configuration (for Tables 1 & 2):**

- Pooling: For each of $N_{\text{res}} = 273$ residues, embeddings ($d_z = 4$) were pooled to $d'_p = 1 \times W = 1 \times 4 = 4$.

I.6 Latent Diffusion Models: Configuration and Training Overview

The Denoising Diffusion Probabilistic Models (DDPMs) [47], as outlined in Appendix D, were implemented to operate on the pooled latent embeddings \mathbf{h}_0 derived from each specific pooling strategy (with dimensions $d_p = 100$ for Blind, $d_p = 135$ for Sequential Backbone, $d_p = 108$ for Sequential Sidechain, and $d_p = 1092$ for Residue, as detailed in Section I.5). Prior to input, these \mathbf{h}_0 embeddings were normalized (zero mean, unit variance) based on statistics from the training set.

Denoising Network Architectures (ϵ_θ) The primary denoising network used for generating the main paper results was a multi-layer perceptron, `DiffusionMLP_v2`, consisting of four linear layers with ReLU activations. This network takes the flattened, noisy latent vector \mathbf{h}_t concatenated with the normalized timestep t/T as input.

- For **Blind Pooling** ($d_p = 100$) and **Sequential Pooling** (for both backbone $d_{p,bb} = 135$ and sidechain $d_{p,sc} = 108$ latents, typically handled by separate diffusion models or a model adapted for the concatenated dimension if combined), the MLP hidden dimension was set to 1024.
- For **Residue Pooling** (operating on the effective concatenated input of $d_p = 1092$), the MLP hidden dimension was increased to 4096 to accommodate the larger input dimensionality.

Alternative MLP architectures (e.g., DiffusionMLP, DiffusionMLP_v3 with varying layer counts and hidden sizes) and a DiffusionConv2D model (treating the pooled latent as an image-like tensor) were also explored, particularly during the hyperparameter scans for the Blind Pooling strategy (see Section I.8).

Diffusion Process and Training Details The DDPMs were trained by minimizing the MSE loss between the true and predicted noise (Eq. 2).

- **Variance Schedule:** A linear variance schedule was used for β_t , progressing from β_{start} to β_{end} over T timesteps.
- **Key Hyperparameters (Typical Values for Main Results):**
 - Total diffusion timesteps (T): Commonly set around 500 (e.g., for Blind/Sequential) or higher (e.g., 1500 for Residue, reflecting findings from grid searches).
 - β_{start} : Typically 5×10^{-6} or 0.005.
 - β_{end} : Typically 0.02 or 0.1.

Specific optimal values were determined through grid searches, examples of which are shown in Section I.8.

- **Optimization:** The Adam optimizer was used with a learning rate typically set to 1×10^{-5} .
- **Training Epochs:** Blind and Sequential pooling diffusion models were trained for approximately 3,000-10,000 epochs. The Residue pooling diffusion model, with its larger latent space, often required more extensive training, up to 150,000 epochs or more, to converge.
- **Data Handling:** Pooled latent embeddings (\mathbf{h}_0) were generated from the entire training set using the best-performing frozen encoder and the respective trained decoder’s pooling mechanism, then saved to HDF5 files for efficient loading during diffusion model training. For Residue pooling, this involved concatenating the N_{res} per-residue pooled vectors for each frame.
- **Checkpointing:** Model checkpoints were saved periodically (e.g., every 50 or 100 epochs) to select the best performing model based on validation metrics (if a validation set of latents was used) or training loss convergence. For Residue pooling, which benefited from multi-epoch sampling for visualization (Appendix H), more frequent checkpointing was sometimes employed.

Sampling New latent embeddings $\mathbf{h}_0^{\text{gen}}$ were generated by the trained ϵ_θ model using the ancestral sampling procedure described in Algorithm 2. These sampled latents were then un-normalized (using the saved training set statistics) before being passed to the corresponding frozen decoder to generate all-atom coordinates $X_{\text{pred}}^{\text{gen}}$.

I.7 Blind Pooling Decoder Hyperparameter Scan Results

Full test set Mean Squared Error (MSE) results (MSE_{bb} for backbone, MSE_{sc} for sidechain) for the 50 Blind Pooling decoder configurations tested for each encoder latent dimension ($d_z \in \{4, 8, 16\}$) are presented in Tables 8-10. These experiments systematically varied the pooling height (H), pooling width (W), and the number of layers in the prediction MLP ($D \equiv N_{\text{layers}}$).

Table 8: Extended Technical Appendix: Full blind pooling Decoder Test MSE Results ($d_z = 4$).

H	W	N_{layers}	MSE_{bb}	MSE_{sc}
10	1	12	0.2520	0.7303
10	2	4	0.1834	0.5825
10	2	8	0.1673	0.5212
15	1	12	0.1965	0.5815
15	1	8	0.2092	0.5998
15	2	4	0.1405	0.4809
15	2	8	0.1820	0.5614
20	1	8	0.1845	0.5507
20	2	4	0.1257	0.4462
20	3	12	0.1081	0.4075
25	1	12	0.1737	0.5146
30	2	4	0.1038	0.3974
30	2	8	0.1064	0.3979
30	3	12	0.0910	0.3712
30	3	4	0.0931	0.3793
35	3	12	0.0888	0.3620
35	3	4	0.0905	0.3614
40	1	12	0.1504	0.4688
40	2	12	0.1006	0.3791
45	1	8	0.1513	0.4630
50	1	12	0.1477	0.4535
50	1	8	0.1442	0.4501
50	2	12	0.0978	0.3705
50	3	8	0.0783	0.3341
55	1	12	0.1492	0.4465
55	1	4	0.1466	0.4461
55	1	8	0.1488	0.4488
55	3	8	0.0820	0.3320
5	1	8	0.4069	1.1194
5	3	8	0.2970	0.8042
60	2	12	0.0884	0.3439
60	3	4	0.0777	0.3159
65	2	4	0.0989	0.3617
65	3	12	0.0791	0.3221
70	1	8	0.1417	0.4279
70	2	12	0.0940	0.3475
75	2	8	0.0919	0.3454
75	3	8	0.0837	0.3211
80	2	4	0.0994	0.3441
85	1	12	0.1427	0.4171
85	1	4	0.1344	0.4082
85	3	4	0.0812	0.3143
85	3	8	0.0815	0.3100
90	1	4	0.1396	0.4112
90	3	4	0.0809	0.3081
90	3	8	0.0794	0.3013
95	1	8	0.1378	0.4088
95	2	12	0.0819	0.3109
95	2	4	0.0973	0.3317
95	3	12	0.0740	0.2926

Table 9: Extended Technical Appendix: Full Blind Pooling Decoder Test MSE Results ($d_z = 8$).

H	W	N_{layers}	MSE_{bb}	MSE_{sc}
100	1	8	0.1393	0.4227
100	2	12	0.1022	0.3531
100	3	4	0.1640	0.4863
100	5	8	0.0744	0.2935
100	7	12	0.0840	0.3013
10	2	12	0.1704	0.5434
15	1	4	0.2284	0.6786
15	1	8	0.2323	0.7050
15	4	8	0.1288	0.4483
15	5	4	0.1173	0.4283
15	6	4	0.1252	0.4360
20	5	8	0.0968	0.3849
25	1	12	0.1878	0.5622
25	4	8	0.1044	0.3991
25	7	4	0.1005	0.3880
35	1	4	0.1677	0.5122
35	2	4	0.1065	0.3973
35	2	8	0.1064	0.3959
35	6	8	0.0874	0.3569
40	2	4	0.1008	0.3852
40	5	8	0.0806	0.3443
45	1	12	0.1610	0.4846
50	1	4	0.1598	0.4785
50	3	12	0.1274	0.4183
50	5	12	0.0767	0.3290
50	6	12	0.0842	0.3432
55	2	8	0.1003	0.3711
55	5	4	0.0729	0.3135
55	6	8	0.0879	0.3459
5	1	12	0.3740	1.0205
5	2	12	0.2496	0.7218
5	4	8	0.2107	0.6336
5	7	8	0.2631	0.7695
60	1	12	0.1494	0.4528
60	3	4	0.1375	0.4204
60	5	4	0.0735	0.3114
65	5	8	0.0724	0.3072
70	2	4	0.0924	0.3475
70	2	8	0.0952	0.3547
70	3	12	0.1671	0.4741
75	1	12	0.1461	0.4409
75	4	12	0.0831	0.3242
80	1	4	0.1422	0.4347
80	2	8	0.0909	0.3364
85	1	12	0.1485	0.4374
90	5	8	0.0747	0.2947
95	1	12	0.1404	0.4253
95	4	8	0.0891	0.3212
95	5	4	0.0730	0.2876
95	6	8	0.0796	0.3036

Table 10: Extended Technical Appendix: Full Blind Pooling Decoder Test MSE Results ($d_z = 16$).

H	W	N_{layers}	MSE_{bb}	MSE_{sc}
100	15	4	0.0858	0.3033
100	2	12	0.0933	0.3349
100	5	4	0.0792	0.2984
100	7	4	0.0734	0.2837
10	10	12	0.1243	0.4333
10	3	8	0.1725	0.5446
10	9	12	0.1329	0.4545
15	14	8	0.1205	0.4164
15	1	12	0.2228	0.6437
15	3	12	0.1506	0.4957
15	7	4	0.1129	0.4104
20	12	4	0.1012	0.3890
20	13	8	0.1190	0.4311
30	12	12	0.0879	0.3680
30	5	8	0.0846	0.3538
35	11	12	0.0934	0.3649
40	15	12	0.0912	0.3521
40	6	12	0.0746	0.3294
40	9	12	0.0783	0.3328
45	11	12	0.0835	0.3447
45	3	8	0.1040	0.3805
45	6	8	0.0759	0.3289
50	2	12	0.1102	0.3934
50	6	12	0.0718	0.3170
50	7	12	0.0759	0.3265
50	9	12	0.0751	0.3236
55	10	4	0.0808	0.3271
55	11	4	0.0786	0.3163
55	12	8	0.0791	0.3243
55	15	4	0.0795	0.3259
55	4	8	0.0890	0.3470
55	7	8	0.0728	0.3107
5	13	12	0.1901	0.5524
60	10	4	0.0734	0.3047
60	4	4	0.0833	0.3386
60	6	8	0.0699	0.3002
60	9	12	0.0803	0.3196
65	4	4	0.0827	0.3329
70	8	4	0.0846	0.3238
70	9	12	0.0817	0.3218
75	5	8	0.0714	0.2992
80	11	12	0.0790	0.3069
80	4	12	0.0815	0.3219
80	5	8	0.0717	0.2981
85	11	4	0.0797	0.2999
90	10	8	0.0724	0.2820
90	12	4	0.0758	0.2919
90	4	4	0.0780	0.3140
90	6	4	0.0690	0.2854
95	9	4	0.0802	0.2987

I.8 Diffusion Model Hyperparameter Scans: Blind Pooling

Extensive hyperparameter optimization was performed for the latent diffusion models across the different pooling strategies and denoiser architectures detailed above. For brevity, and to illustrate the typical scope of these optimizations, the detailed tables that follow (Tables 11-16) focus on presenting results for the **Blind Pooling** strategy. These tables showcase performance across varying encoder latent dimensions ($d_z \in \{4, 8, 16\}$), for both MLP (specifically DiffusionMLP_v2) and Conv2D denoiser architectures, against a grid of diffusion hyperparameters (total timesteps T , β_{start} , and β_{end}). While not all combinations are exhaustively tabulated for every pooling method in this appendix, similar systematic grid search approaches were applied to optimize the Sequential and Residue pooling diffusion models, tailoring parameter ranges and model configurations (e.g., MLP hidden dimensions, training epochs) according to their specific input characteristics and computational demands.

Table 11: Extended Technical Appendix: Full Diffusion Grid Results (blind pooling, $d_z = 4$, $H = 30$, $W = 2$, MLP Denoiser). "(Rec.)" denotes Decoder Reconstruction from ground-truth latents; "(Diff.)" denotes full Diffusion pipeline results.

Exp ID	IDDT _{All} (Rec.)	IDDT _{BB} (Rec.)	TM _{All} (Rec.)	TM _{BB} (Rec.)	IDDT _{All} (Diff.)	IDDT _{BB} (Diff.)	TM _{All} (Diff.)	TM _{BB} (Diff.)
1	0.716	0.792	0.961	0.957	0.651	0.699	0.949	0.936
2	0.717	0.793	0.962	0.957	0.611	0.660	0.938	0.923
3	0.716	0.792	0.961	0.957	0.615	0.661	0.942	0.926
4	0.717	0.793	0.961	0.957	0.621	0.667	0.945	0.932
5	0.714	0.792	0.961	0.957	0.610	0.655	0.938	0.920
6	0.716	0.793	0.961	0.957	0.629	0.679	0.949	0.937
7	0.717	0.792	0.961	0.957	0.531	0.574	0.909	0.880
8	0.716	0.793	0.961	0.957	0.376	0.392	0.773	0.710
9	0.715	0.794	0.961	0.957	0.543	0.583	0.910	0.880
10	0.715	0.793	0.961	0.957	0.495	0.528	0.880	0.842
11	0.717	0.794	0.961	0.957	0.573	0.608	0.922	0.899
12	0.717	0.793	0.961	0.957	0.571	0.607	0.927	0.905
13	0.716	0.793	0.961	0.957	0.594	0.641	0.939	0.922
14	0.714	0.793	0.961	0.957	0.605	0.645	0.936	0.918
15	0.716	0.792	0.961	0.957	0.515	0.542	0.888	0.867

Table 12: Extended Technical Appendix: Full Diffusion Grid Results (blind pooling, $d_z = 4$, $H = 30$, $W = 2$, Conv2D Denoiser). "(Rec.)" denotes Decoder Reconstruction from ground-truth latents; "(Diff.)" denotes full Diffusion pipeline results.

Exp ID	IDDT _{All} (Rec.)	IDDT _{BB} (Rec.)	TM _{All} (Rec.)	TM _{BB} (Rec.)	IDDT _{All} (Diff.)	IDDT _{BB} (Diff.)	TM _{All} (Diff.)	TM _{BB} (Diff.)
1	0.716	0.794	0.961	0.957	0.240	0.244	0.375	0.287
2	0.717	0.792	0.961	0.957	0.239	0.246	0.376	0.286
3	0.714	0.792	0.961	0.957	0.239	0.247	0.375	0.287
4	0.716	0.793	0.961	0.957	0.237	0.244	0.377	0.283
5	0.717	0.793	0.961	0.957	0.237	0.243	0.371	0.282
6	0.717	0.794	0.961	0.957	0.240	0.245	0.375	0.288
7	0.716	0.795	0.961	0.957	0.239	0.244	0.376	0.289
8	0.716	0.793	0.961	0.957	0.236	0.243	0.375	0.284
9	0.715	0.792	0.961	0.957	0.237	0.246	0.379	0.285
10	0.716	0.792	0.961	0.957	0.235	0.243	0.375	0.284
11	0.715	0.794	0.961	0.957	0.236	0.243	0.378	0.287
12	0.716	0.795	0.961	0.957	0.236	0.243	0.379	0.288
13	0.716	0.793	0.961	0.957	0.239	0.245	0.372	0.283
14	0.715	0.794	0.961	0.957	0.235	0.243	0.373	0.282
15	0.718	0.793	0.961	0.957	0.239	0.245	0.377	0.286

Table 13: Extended Technical Appendix: Full Diffusion Grid Results (blind pooling, $d_z = 8$, $H = 35$, $W = 2$, MLP Denoiser). "(Rec.)" denotes Decoder Reconstruction from ground-truth latents; "(Diff.)" denotes full Diffusion pipeline results.

Exp ID	IDDT _{All} (Rec.)	IDDT _{BB} (Rec.)	TM _{All} (Rec.)	TM _{BB} (Rec.)	IDDT _{All} (Diff.)	IDDT _{BB} (Diff.)	TM _{All} (Diff.)	TM _{BB} (Diff.)
1	0.714	0.793	0.961	0.957	0.671	0.728	0.957	0.947
2	0.714	0.792	0.961	0.957	0.634	0.678	0.951	0.935
3	0.715	0.791	0.961	0.957	0.601	0.648	0.944	0.930
4	0.715	0.792	0.961	0.958	0.663	0.722	0.955	0.945
5	0.715	0.793	0.961	0.957	0.631	0.680	0.951	0.938
6	0.714	0.792	0.961	0.957	0.677	0.733	0.960	0.950
7	0.713	0.793	0.961	0.958	0.669	0.722	0.959	0.949
8	0.715	0.794	0.961	0.957	0.638	0.689	0.953	0.939
9	0.714	0.792	0.961	0.957	0.567	0.603	0.924	0.901
10	0.714	0.792	0.961	0.957	0.613	0.663	0.945	0.931
11	0.715	0.793	0.961	0.957	0.631	0.682	0.951	0.939
12	0.715	0.793	0.961	0.957	0.628	0.676	0.954	0.941
13	0.715	0.793	0.961	0.957	0.652	0.709	0.954	0.943
14	0.713	0.793	0.961	0.957	0.567	0.605	0.937	0.917
15	0.712	0.793	0.961	0.957	0.425	0.446	0.865	0.817

Table 14: Extended Technical Appendix: Full Diffusion Grid Results (blind pooling, $d_z = 8$, $H = 35$, $W = 2$, Conv2D Denoiser). "(Rec.)" denotes Decoder Reconstruction from ground-truth latents; "(Diff.)" denotes full Diffusion pipeline results.

Exp ID	IDDT _{All} (Rec.)	IDDT _{BB} (Rec.)	TM _{All} (Rec.)	TM _{BB} (Rec.)	IDDT _{All} (Diff.)	IDDT _{BB} (Diff.)	TM _{All} (Diff.)	TM _{BB} (Diff.)
1	0.713	0.792	0.961	0.957	0.243	0.252	0.376	0.285
2	0.715	0.792	0.961	0.957	0.240	0.248	0.373	0.283
3	0.715	0.792	0.961	0.958	0.241	0.248	0.373	0.281
4	0.715	0.794	0.961	0.958	0.241	0.248	0.372	0.286
5	0.713	0.790	0.961	0.958	0.242	0.250	0.375	0.287
6	0.715	0.793	0.961	0.957	0.245	0.251	0.378	0.294
7	0.714	0.792	0.961	0.957	0.239	0.248	0.366	0.276
8	0.714	0.794	0.961	0.957	0.239	0.245	0.366	0.276
9	0.715	0.792	0.961	0.957	0.239	0.247	0.367	0.282
10	0.715	0.793	0.961	0.957	0.236	0.245	0.356	0.268
11	0.714	0.793	0.961	0.957	0.240	0.248	0.372	0.282
12	0.715	0.793	0.961	0.957	0.240	0.250	0.373	0.284
13	0.714	0.794	0.961	0.957	0.239	0.249	0.371	0.279
14	0.714	0.792	0.961	0.957	0.240	0.247	0.366	0.278
15	0.714	0.794	0.961	0.958	0.242	0.251	0.368	0.283

Table 15: Extended Technical Appendix: Full Diffusion Grid Results (blind pooling, $d_z = 16$, $H = 50$, $W = 2$, MLP Denoiser). "(Rec.)" denotes Decoder Reconstruction from ground-truth latents; "(Diff.)" denotes full Diffusion pipeline results.

Exp ID	IDDT _{All} (Rec.)	IDDT _{BB} (Rec.)	TM _{All} (Rec.)	TM _{BB} (Rec.)	IDDT _{All} (Diff.)	IDDT _{BB} (Diff.)	TM _{All} (Diff.)	TM _{BB} (Diff.)
1	0.714	0.792	0.961	0.957	0.709	0.780	0.962	0.957
2	0.715	0.790	0.961	0.957	0.707	0.781	0.962	0.958
3	0.716	0.791	0.961	0.956	0.706	0.779	0.961	0.954
4	0.714	0.792	0.961	0.957	0.719	0.792	0.964	0.960
5	0.713	0.791	0.961	0.957	0.703	0.775	0.962	0.957
6	0.717	0.791	0.961	0.957	0.706	0.780	0.961	0.955
7	0.715	0.791	0.961	0.957	0.702	0.769	0.962	0.956
8	0.716	0.791	0.961	0.957	0.697	0.758	0.960	0.952
9	0.717	0.791	0.961	0.957	0.698	0.763	0.964	0.958
10	0.715	0.791	0.961	0.957	0.688	0.755	0.960	0.952
11	0.715	0.792	0.961	0.957	0.689	0.752	0.959	0.950
12	0.714	0.792	0.961	0.956	0.704	0.772	0.960	0.953
13	0.715	0.794	0.961	0.957	0.699	0.766	0.962	0.954
14	0.715	0.793	0.961	0.956	0.690	0.750	0.960	0.953
15	0.715	0.791	0.961	0.957	0.677	0.740	0.957	0.948

Table 16: Extended Technical Appendix: Full Diffusion Grid Results (blind pooling, $d_z = 16$, $H = 50$, $W = 2$, Conv2D Denoiser). "(Rec.)" denotes Decoder Reconstruction from ground-truth latents; "(Diff.)" denotes full Diffusion pipeline results.

Exp ID	IDDT _{All} (Rec.)	IDDT _{BB} (Rec.)	TM _{All} (Rec.)	TM _{BB} (Rec.)	IDDT _{All} (Diff.)	IDDT _{BB} (Diff.)	TM _{All} (Diff.)	TM _{BB} (Diff.)
1	0.714	0.791	0.961	0.957	0.261	0.267	0.397	0.305
2	0.715	0.790	0.961	0.957	0.263	0.270	0.399	0.308
3	0.714	0.791	0.961	0.957	0.263	0.270	0.404	0.312
4	0.715	0.792	0.961	0.957	0.264	0.270	0.404	0.309
5	0.717	0.792	0.961	0.957	0.261	0.266	0.401	0.308
6	0.713	0.792	0.961	0.957	0.262	0.270	0.399	0.306
7	0.716	0.793	0.961	0.957	0.262	0.269	0.397	0.309
8	0.715	0.791	0.961	0.957	0.264	0.269	0.405	0.314
9	0.716	0.792	0.961	0.957	0.266	0.272	0.406	0.314
10	0.715	0.791	0.961	0.957	0.261	0.269	0.402	0.307
11	0.714	0.792	0.961	0.957	0.265	0.270	0.406	0.311
12	0.715	0.793	0.961	0.957	0.262	0.271	0.404	0.312
13	0.716	0.792	0.961	0.957	0.266	0.274	0.403	0.312
14	0.713	0.792	0.961	0.957	0.260	0.268	0.395	0.307
15	0.716	0.792	0.961	0.957	0.263	0.270	0.406	0.306

I.9 Conditioning Mechanism Tuning

As detailed in Section 3.2 (Conditioning Mechanism paragraph), the decoder component of LD-FPG is conditioned on information derived from a reference structure, X_{ref} . Our primary conditioning strategy utilizes the latent representation of this reference, $C = Z_{\text{ref}} = \Theta^*(X_{\text{ref}}, E_{\text{ref}})$, obtained from the pre-trained and frozen encoder Θ^* . This choice was motivated by preliminary findings suggesting its superiority over direct conditioning on raw Cartesian coordinates, $C = X_{\text{ref}}$.

To rigorously validate this and quantify the performance difference, we conducted comprehensive ablation studies. These studies compared models conditioned on Z_{ref} (indicated by the `_zref` suffix in their experimental set identifiers) against baseline models conditioned on X_{ref} . The comparisons spanned different architectural configurations of the decoder, including:

- **Pooling Strategy:** Experiments were run using both Blind Pooling and Residue Pooling decoders, as described in Section 3.3. The Residue Pooling strategy itself had variants explored: a standard Residue (1level) application and a hierarchical Residue (2level)

approach. In the Residue (2level) configuration, the processing involved a two-stage pooling scheme: atom-wise latent embeddings $Z^{(t)}$ first underwent a global blind pooling operation. The output context vector from this initial global pooling was then subsequently used as an input or integrated within a residue-specific pooling or processing mechanism before the final MLP prediction for each residue’s atoms.

- **Cross-Attention (CA):** For some configurations, a Cross-Attention mechanism (denoted `_CA_on`) was employed. This module, defined as:

```
class CrossAttentionBlock(nn.Module):
    def __init__(self, q_dim, kv_dim, att_dim=64):
        super().__init__(); self.s = att_dim**-0.5
        self.q=nn.Linear(q_dim,att_dim,bias=False)
        self.k=nn.Linear(kv_dim,att_dim,bias=False)
        self.v=nn.Linear(kv_dim,att_dim,bias=False)
    def forward(self, q, k, v):
        Q=self.q(q); K=self.k(k); V=self.v(v)
        sc = torch.matmul(Q, K.transpose(-1, -2)) * self.s
        return torch.matmul(F.softmax(sc, dim=-1), V)
```

allows the pooled latent embeddings derived from the input dynamic conformation (\mathbf{h}_0) to interact with and selectively integrate information from the reference structure representation (e.g., Z_{ref}). Configurations without this mechanism (`_CA_off`) typically use simpler concatenation or direct feeding of \mathbf{h}_0 and the conditioner to the subsequent MLP.

It is important to note that these ablation studies comparing conditioning mechanisms were conducted with other architectural and training hyperparameters (beyond those swept for $H, W, H2, W2$ within each group, such as encoder specifics or base learning rate schedules) fixed to a representative set; this foundational parameter set is not discussed in detail here.

The optimizer was generally Adam, except for one set of experiments explicitly testing AdamW (e.g., `blind_res_CA_off_zref_lr.Adamw`). The primary metric for comparison was the minimum test loss achieved across an extensive hyperparameter search (varying decoder-specific pooling dimensions H, W and MLP architecture parameters $H2, W2$) within each experimental group.

Table 17: Ablation Study Results for Decoder Conditioning Mechanism. Performance is compared based on minimum test loss. ‘ X_{ref} Cond.’ refers to conditioning on raw Cartesian coordinates, while ‘ Z_{ref} Cond.’ refers to conditioning on latent reference embeddings. “1level” and “2level” refer to specific variants of the Residue Pooling architecture, with “2level” involving an initial global blind pooling stage prior to residue-specific processing.

Pooling	Cross-Attention	X_{ref} Cond.	Z_{ref} Cond.	Improvement (%)
Blind	Off	0.7763 (15)	0.5327 (32)	31.4
Blind	On	1.6787 (16)	0.5835 (24)	65.2
Residue	On	1.2417 (6)	0.2453 (14)	80.2
Residue (1level)	Off	0.2290 (19)	0.1058 (10)	53.8
Residue (2level)	Off	0.7599 (20)	0.5749 (49)	24.3

The results presented in Table 17 consistently show that conditioning on the latent reference embeddings (Z_{ref}) leads to substantially lower minimum test losses compared to conditioning on raw Cartesian coordinates (X_{ref}). This performance advantage holds across both Blind and Residue pooling strategies (including its “1level” and “2level” variants) and is evident whether Cross-Attention is used or not. For instance, with Blind Pooling and CA off, Z_{ref} conditioning achieved a $\sim 31.4\%$ lower loss. This effect was even more pronounced for Residue Pooling (CA On), where an $\sim 80.2\%$ improvement was observed. Even for the more complex Residue (2level) architecture, Z_{ref} conditioning provided a notable $\sim 24.3\%$ reduction in loss.

The single experimental group `blind_res_CA_off_zref_lr.Adamw` (16 runs, Min Test Loss 0.7592), which used Z_{ref} conditioning with the AdamW optimizer, yielded a higher loss than its Adam-optimized counterpart (`blind_res_CA_off_zref`, Min Test Loss 0.5327). While this suggests that Adam may have been more suitable or better tuned for this particular setup, it does not

detract from the central finding regarding the conditioning variable itself, as no corresponding X_{ref} -conditioned AdamW experiments were available for direct comparison.

In conclusion, these ablation studies provide robust quantitative evidence supporting the design choice of using the encoder-derived latent representation Z_{ref} as the primary conditioning mechanism for the decoder in LD-FPG. This strategy enables the model to more effectively learn and represent conformational deformations relative to a well-characterized reference state, leading to improved generative performance.

L.10 Discussion on Metric Variability and Standard Deviations

Throughout this paper, our evaluation process involves training each model component (encoder, decoder, diffusion model) and then assessing its performance by generating an ensemble of protein conformations. These generated ensembles are then compared against the reference Molecular Dynamics (MD) ensemble, with key metrics such as IDDT, TM-score, and Jensen-Shannon Divergence (JSD) for dihedral angles reported. For clarity and conciseness, the main summary tables (e.g., Table 1 and Table 2) present the mean values for per-structure metrics like IDDT and TM-score. This section provides further context on the variability observed in these metrics, typically characterized by their standard deviations (SD).

While standard deviations for metrics like IDDT and TM-score offer insight into the spread of structural quality within an ensemble, we argue that the $\sum \text{JSD}$ values for backbone and side-chain dihedral angles (reported directly in Tables 1 and 2) serve as a more direct and potent indicator of how well the *distributional variability* and local conformational diversity of the reference MD ensemble are captured. A low $\sum \text{JSD}$ signifies that the variety and relative populations of local backbone (ϕ, ψ) and side-chain (χ) conformations in the generated ensemble closely mirror those of the MD data. Furthermore, qualitative assessments of landscape coverage, such as the Principal Component Analysis (PCA) of latent embeddings (Figure 4, top row) and the A100 activation index distributions (Figure 4, bottom row), provide richer, more nuanced views of overall conformational diversity and the exploration of functionally relevant states than a single SD value of a global structural similarity score might offer.

Nevertheless, to provide a comprehensive picture, we report the observed standard deviations for IDDT_{All} and $\text{TM-score}_{\text{All}}$ across different stages of our pipeline, calculated over the entire test set ensemble for each respective model configuration:

- **IDDT_{All} Standard Deviations:**

- Ground Truth MD Ensemble (vs. X_{ref}): $\text{SD} \approx 0.028$
- ChebNet Encoder Reconstruction Head (Table 3): $\text{SD} \approx 0.030$
- Decoder-Generated Ensembles (Table 1, from ground-truth latents):
 - * Blind Pooling ($d_z = 16$): $\text{SD} \approx 0.031$
 - * Sequential Pooling ($d_z = 8$): $\text{SD} \approx 0.032$
 - * Residue Pooling ($d_z = 4$): $\text{SD} \approx 0.040$
- Diffusion-Generated Ensembles (Table 2):
 - * Blind Pooling: $\text{SD} \approx 0.042$
 - * Sequential Pooling: $\text{SD} \approx 0.058$
 - * Residue Pooling: $\text{SD} \approx 0.091$

- **TM-score_{All} Standard Deviations:**

- Ground Truth MD Ensemble (vs. X_{ref}): $\text{SD} \approx 0.0059$
- ChebNet Encoder Reconstruction Head (Table 3): $\text{SD} \approx 0.0060$
- Decoder-Generated Ensembles (Table 1):
 - * Blind Pooling ($d_z = 16$): $\text{SD} \approx 0.0062$
 - * Sequential Pooling ($d_z = 8$): $\text{SD} \approx 0.0065$
 - * Residue Pooling ($d_z = 4$): $\text{SD} \approx 0.020$
- Diffusion-Generated Ensembles (Table 2):
 - * Blind Pooling: $\text{SD} \approx 0.015$
 - * Sequential Pooling: $\text{SD} \approx 0.025$

* Residue Pooling: $SD \approx 0.048$

These standard deviations were computed by evaluating the respective metric for each structure in the generated test ensemble against the reference structure (X_{ref}) and then calculating the standard deviation of these scores. The Python script provided (calc_iddt.py) illustrates the methodology for calculating such mean and standard deviation values for IDDT scores over an ensemble, including options for subsampling if required for very large datasets.

Interpreting these SD values: The SDs for IDDT and TM-score for the ChebNet encoder and the decoder-generated ensembles (from ground-truth latents) are generally low and quite comparable to the inherent variability observed within the ground truth MD ensemble itself when compared against the static X_{ref} . This indicates that the encoder and decoders maintain a consistent level of structural fidelity. For the diffusion-generated ensembles, the SD values, particularly for IDDT, show a modest increase. For instance, the SD for IDDT_{All} ranges from approximately 0.04 to 0.09. This suggests a slightly greater degree of structural heterogeneity in the ensembles produced by the full generative pipeline compared to the direct decoder outputs or the original MD data’s deviation from X_{ref} . This increased spread can be acceptable, or even indicative of the model exploring the learned conformational manifold, as long as the mean fidelity remains high (as reported in Table 2) and, crucially, the critical distributional features of the ensemble (captured by $\sum \text{JSD}$ for dihedrals and A100 landscape analysis) are well-reproduced. The very low SDs for TM-score across all stages consistently affirm that the global fold of the protein is well-preserved.

In summary, while mean values are prioritized in the main tables for direct comparison of central tendencies, the analysis of $\sum \text{JSD}$ for dihedral distributions, PCA of latent spaces, A100 activation profiles, and the contextualized standard deviations discussed here collectively provide a comprehensive assessment of both the fidelity and the diversity of the conformational ensembles generated by LD-FPG.